

QUANTUM WELL DEVICES FABRICATED USING SELECTIVE AREA
GROWTH AND THEIR APPLICATION IN OPTICAL FIBER
COMMUNICATION

BY

PAVEL LIUDVIH

THESIS

Submitted in partial fulfillment of the requirements
for the degree of Master of Science in Electrical and Computer Engineering
in the Graduate College of the
University of Illinois at Urbana-Champaign, 2013

Urbana, Illinois

Adviser:

Professor Emeritus James J. Coleman

ABSTRACT

In this thesis we discuss the advantage of the selective area growth (SAG) approach to manufacturing integrated quantum-well lasers and modulators.

SAG can be successfully achieved with two major growth techniques: metalorganic chemical vapor deposition (MOCVD) and molecular beam epitaxy (MBE). We will put more weight on SAG with MOCVD growth because certain properties of this technique are particularly attractive. We summarize growth conditions including pressure, temperature, material supply rate, and ratio of source materials for optimum SAG results. By adjusting the dielectric mask geometry one can simultaneously grow photonic devices with a range of absorption/emission spectra on the same substrate. We will introduce a theoretical SAG model and apply it to both discrete and integrated III-V compound semiconductor photonic devices. The prediction is compared with the experimental results and discussed in details.

ACKNOWLEDGMENTS

First and foremost, I would like to thank Professor James Coleman for his tireless support and patience as I was making my, occasionally clumsy, way through graduate school. Thank you for your continued faith in humanity and for keeping your door open both literally and figuratively. Thank you for not only educating your students, but also for mentoring them.

I also would like to thank Professor Ann Catrina Coleman – the first person from the University of Illinois to reach out to me and give an interview. Thank you for providing your feedback and sharing your experience during our meetings.

I would like to thank Professor Oliver Chen for his advice on my academic writing. I realize it is still far from perfect, but it is definitely much better than before. My special thanks go to people I spent the most time with: Jeong Dong Kim (JD), Nick Choi, Yun Lu, and Joseph Zimmerman. Thank you for training me on our manufacturing and test equipment. The four of you along with Runyu Liu and Shiul Khadka defined, for the most part, my entire social life between August 2012 and December 2013.

I am greatly obliged to my mother for her support and wisdom. She always advocated for higher education and I am glad I took her advice. Thank you, Mom.

CONTENTS

1. INTRODUCTION	1
1.1 Photonic Devices and Their Application in Signal Processing	1
1.2 Motivation for QW Structures	5
1.2.1 Quantized Energy States	5
1.2.2 Strained QW and Multiple QW	8
2. SELECTIVE AREA GROWTH (SAG)	12
2.1 SAG Using Metalorganic Chemical Vapor Deposition (MOCVD)	12
2.2 Molecular Beam Epitaxy (MBE)	21
3. SELECTIVELY GROWN PHOTONIC QW DEVICES	28
3.1 QW Laser	28
3.1.1 Theory of QW Laser	28
3.1.2 Buried Heterostructure (BH) Laser	31
3.2 Electro-Absorption Modulator (EAM)	33
3.3 Integrating a QW Laser and EAM	36
4. CONCLUSION AND FUTURE PERSPECTIVES	38
APPENDIX A – $\text{Al}_x\text{Ga}_y\text{In}_{1-x-y}\text{As}$ BANDGAP CALCULATION	40
APPENDIX B – DENSITY OF STATES	42
REFERENCES	44

1. INTRODUCTION

1.1 Photonic Devices and Their Application in Signal Processing

According to the Merriam-Webster dictionary, photonics is a branch of physics that deals with the properties and applications of photons, especially as a medium for information transmission. Applications of photonics today are ubiquitous and include optical fiber communication, data storage, solid state lighting, solar energy, and others. Photon generation, modulation, and detection can be performed with high conversion efficiency by the photonic devices made from direct bandgap semiconductor materials. Electron-hole generation and recombination in such materials happen without a significant change of the carrier momentum. Several material systems from the III-V and II-VI compounds have been extensively studied and exhibit very attractive properties for serving as an integrated photonic device platform. Recent advancements in the semiconductor industry have made it possible to manufacture high-quality photonic devices. In particular, metalorganic chemical vapor deposition (MOCVD) and molecular beam epitaxy (MBE) can be used to grow high-quality planar devices with monoatomic layer accuracy. Both methods will be discussed in greater detail in Chapter 2.

One area particularly benefiting from the usage of photonic devices is optical fiber communication. Optical fiber communication systems have replaced copper wire in many core networks and play an essential role in high speed data transfer [1] mainly due to high channel capacity, extremely low crosstalk, and immunity to electro-magnetic interference. This thesis will focus on some of the recent advancements in the electro-optical components of such communication systems. The three main modules of the system include the transmitter, the

optical fiber, and the receiver. In the transmitter, our components of interest are the light source and the modulator. While several kinds of light-emitting devices can serve as light sources, the function usually falls to laser diodes due to the superior properties of light beam they generate. The modulator is then used to add useful information onto the carrier beam from the source by modulating the amplitude, phase, polarization, and frequency of the beam. An optical fiber serves as a transmission medium for the signal and is commonly made from silica.

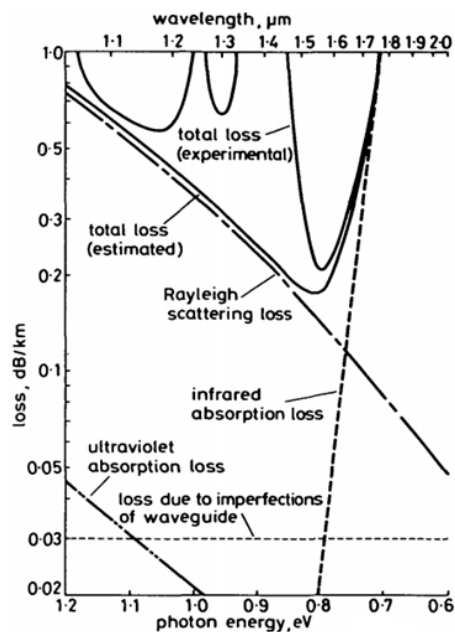


Figure 1-1. Transmission loss mechanism in optical fiber [2].

Silica glass used in waveguide manufacturing is cheap and robust; however, it limits the optical system operation to several optical windows in the near-IR region (Figure 1-1) [2]. A light source and a modulator of such system are thus made from the material capable of generating and modulating light in the near-IR region. Most communication networks operate at around 1.55 μm wavelengths because of low signal loss and they utilize compensator modules to deal with dispersion produced by the silica.

Although most long-haul transmission channels operate at around 1.55 μm , several other optical windows are also important for optical communications. One such window is around 1.3 μm , where an optical fiber has zero dispersion. Another important wavelength for the optical communication system is around 980 nm. Lasers operating at this wavelength are used to pump the erbium-doped fiber amplifier (EDFA), which, in turn, is used to amplify the signal in the optical fiber after it travels a certain distance to compensate for the propagation loss [3]. Photonic devices operating at 980 nm, 1.3 μm and 1.55 μm must have energy transitions at 1.26 eV, 0.95 eV and 0.80 eV respectively. Energy transitions in a semiconductor photonic device depend on its structure and material, which is often a III-V compound.

Photonic devices operating at 980 nm are frequently fabricated from $\text{Ga}_x\text{In}_{1-x}\text{As}$ alloy on the GaAs substrate [4], [5] using one of the epitaxial growth techniques discussed in Chapter 2. Bandgap of a bulk $\text{Ga}_x\text{In}_{1-x}\text{As}$ is calculated by Goetz et al. [6] to be between 0.36 eV and 1.42 eV depending on the alloy composition :

$$E_{g,bulk}(\text{Ga}_x\text{In}_{1-x}\text{As}) = 0.36 + 0.63x + 0.43x^2 \text{ eV} \quad (1.1)$$

Depending on the composition, $\text{Ga}_x\text{In}_{1-x}\text{As}$ alloy will also have different lattice constant according to Vegard's law:

$$a_0(\text{Ga}_x\text{In}_{1-x}\text{As}) = xa_{\text{GaAs}} + (1-x)a_{\text{InAs}} \quad (1.2)$$

where a_{GaAs} and a_{InAs} are the lattice constants of GaAs and InAs respectively. Today's fabrication methods allow for certain lattice mismatch between the grown epilayer and the substrate without forming defects. Moreover, lattice mismatch is often exploited to perform the bandgap engineering as talked about in Section 1.2.2.

Photonic devices operating at 1.3 μm and 1.5 μm are often fabricated from $\text{In}_{1-x}\text{Ga}_x\text{As}_y\text{P}_{1-y}$ alloy on the InP substrate [7], [8]. Bandgap of the bulk $\text{In}_{1-x}\text{Ga}_x\text{As}_y\text{P}_{1-y}$ depends on the alloy composition as adapted from [9]:

$$E_{g,bulk}(\text{In}_{1-x}\text{Ga}_x\text{As}_y\text{P}_{1-y}) = 1.35 + 0.668x - 1.068y + 0.758x^2 + 0.078y^2 - 0.069xy - 0.322x^2y + 0.03xy^2 \text{ eV at 300 K} \quad (1.3)$$

Figure 1-2 helps to visualize Equation (1.3) and indicates several points of interest. Composition of $\text{In}_{1-x}\text{Ga}_x\text{As}_y\text{P}_{1-y}$ corresponding to indirect bandgap alloy is shown in the right bottom corner. The line from the left bottom corner indicates $\text{In}_{1-x}\text{Ga}_x\text{As}_y\text{P}_{1-y}$ composition when it is lattice matched to InP. Points A and B on this line denote $\text{In}_{1-x}\text{Ga}_x\text{As}_y\text{P}_{1-y}$ composition with bandgaps corresponding to 1.55 μm and 1.3 μm respectively. Consult Appendix A for details on derivation and plotting.

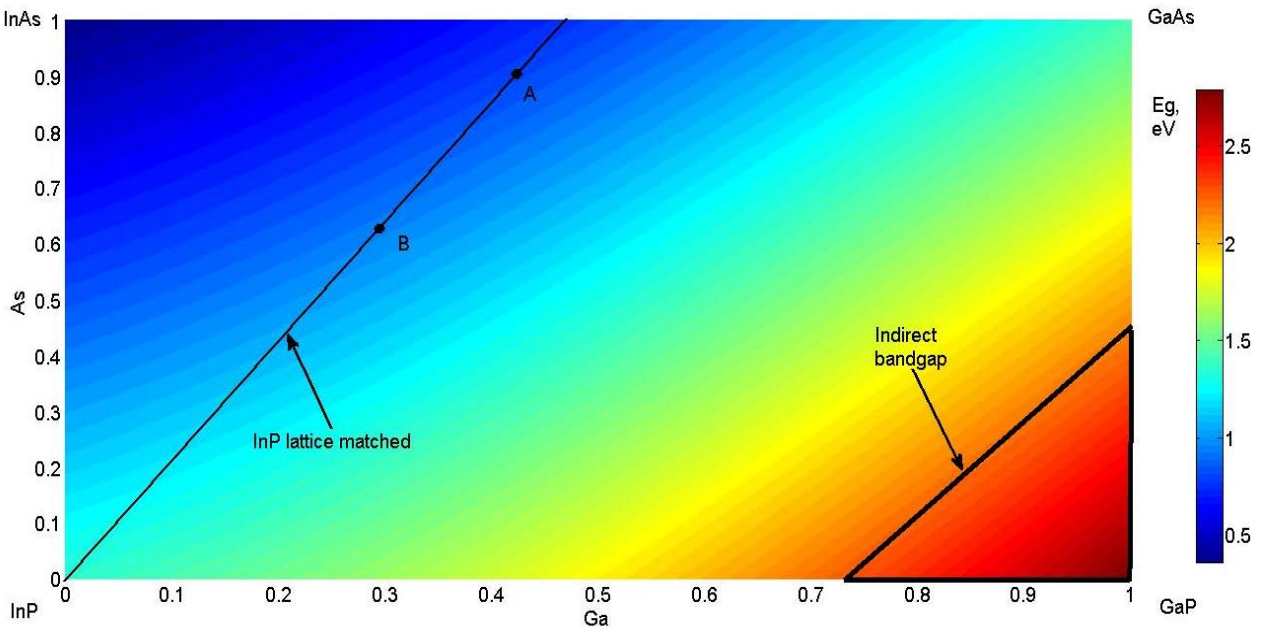


Figure 1-2. InGaAsP compositional plane.

The lattice constant of $\text{In}_{1-x}\text{Ga}_x\text{As}_y\text{P}_{1-y}$ can be found using Vegard's law:

$$a_0(\text{In}_{1-x}\text{Ga}_x\text{As}_y\text{P}_{1-y}) = xy a_{\text{InAs}} + x(1-y)a_{\text{InP}} + y(1-x)a_{\text{GaAs}} + (1-x)(1-y)a_{\text{GaP}} \quad (1.4)$$

where $a_{\alpha\beta}$ is the lattice constant of the binary $\alpha\beta$ alloy. Similarly to the ternary compounds case, the lattice mismatch between the grown epilayer and the substrate can be used to our advantage.

Photonic devices working at 980 nm, 1.3 μm , and 1.55 μm wavelengths are most commonly made using a quantum well (QW) structure as an active region. Active regions of lasers and modulators are the regions respectively designed to enhance light emission and modulation. A QW structure is represented by a narrow bandgap material sandwiched between two wider bandgap materials. When compared to its predecessor, double heterostructure device, QW device benefits from lower threshold current, better thermal stability, wavelength tunability, and several other properties [10]. These properties have motivated extensive QW devices research, which resulted in reliable and commercially available communication components.

1.2 Motivation for QW Structures

1.2.1 Quantized Energy States

As mentioned in Section 1.1, the QW devices offer some advantages over bulk semiconductor devices. These advantages are possible because of spatial confinement of charge carriers within the QW. The thickness of the active region, or the width of a QW, is comparable to the de Broglie wavelength of the carrier. The de Broglie wavelength is defined as

$$\lambda = \frac{h}{p} \quad (1.5)$$

where h is Planck's constant and p is the momentum of the particle. The difference between the energy bandgaps $E_{g, QW}$ and $E_{g, Bulk}$ in Figure 1-3 (a) promotes carrier confinement in 1 dimension, namely the z -direction, allowing the carriers to move freely in the x - and y -directions as shown in Figure 1-3 (b).

The QW can also serve as a waveguide for an optical mode. The approximate relation between the refractive index and the bandgap of a semiconductor has been derived by Gupta and Ravindra [11]:

$$n = 4.16 - 1.12E_g + 0.31E_g^2 - 0.08E_g^3 \quad (1.6)$$

Due to bandgap difference between the QW and the surrounding layers, the resulting index step provides the optical mode confinement, which is often enhanced by fabricating a ridge structure [12].

Another outcome of the carrier confinement is the quantization of the energy states as shown in Figure 1-3 (c). The bulk semiconductor density of states (DOS) (derived in Appendix B) relates to the carrier energy as:

$$\rho_{bulk}(E) \propto \sqrt{E} \quad (1.7)$$

The QW DOS relates to the carrier energy as:

$$\rho_{QW}(E) \propto \sum_n H(E - E_n) \quad (1.8)$$

where $H(E - E_n)$ is the Heaviside step function $H(x) = 1$ for $x > 0$ and $H(x) = 0$ for $x < 0$.

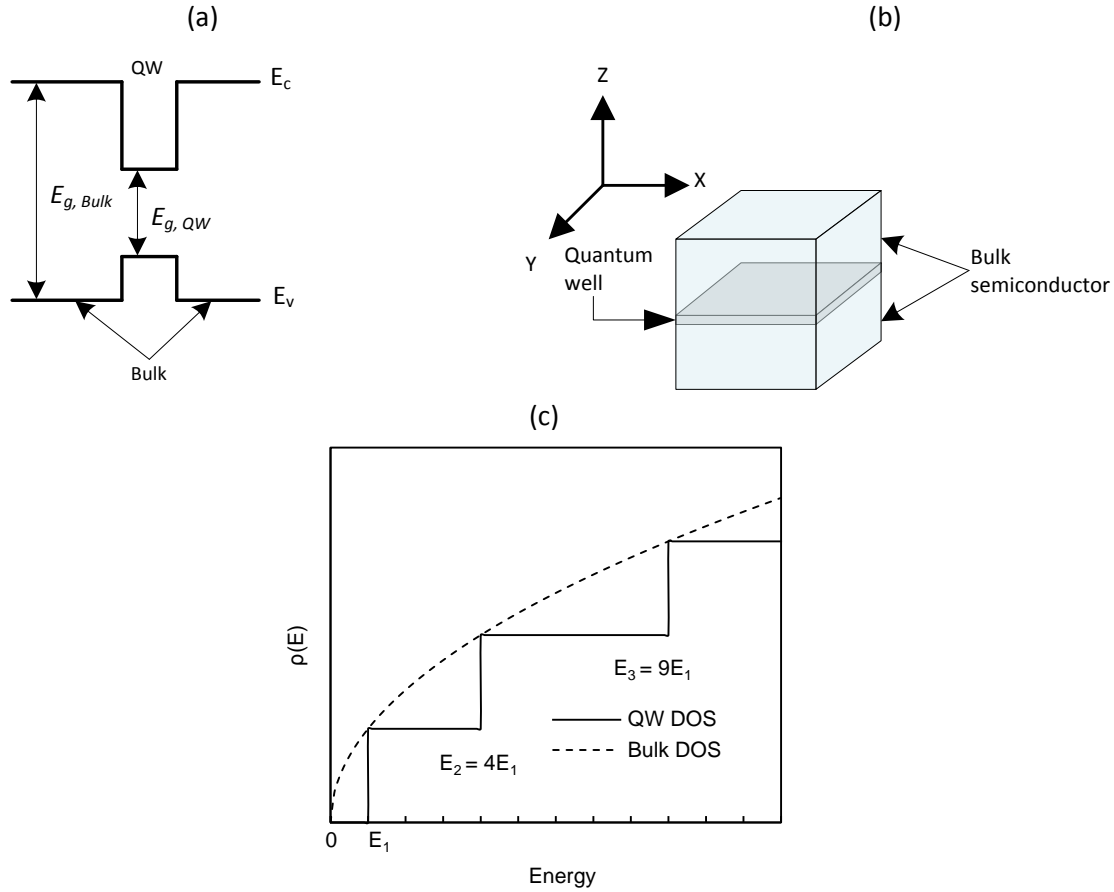


Figure 1-3. (a) QW energy band diagram; (b) QW schematic; (c) related DOS in conduction band.

Figure 1-3 (c) compares the DOS for QW and bulk semiconductor regions. Two features can be noted from this figure: the ground state energy is higher by some value E_1 for the QW; and the QW DOS has a stepwise behavior. These quantized energy levels can be represented by

$$E_n = \frac{\hbar^2}{2m^*} \left(\frac{n\pi}{L} \right)^2 \quad (1.9)$$

where L is the width of the well, m^* is the effective mass of the carrier, \hbar (hbar) is the Planck's constant divided by 2π , and $n=1,2,3\dots$ is the energy level. Thus, the carriers' spatial confinement within the QW leads to quantization of the carriers' energy. Equation (1.9) also shows the energy level value (e.g. E_1) dependence on the width of the QW. The transitions

between the energy levels in a photonic device determine its operating wavelength. Therefore, by choosing the appropriate QW width and composition we can fabricate a photonic device operating at a desired wavelength.

1.2.2 Strained QW and Multiple QW

This section briefly mentions two unique QW features, which are used to select a photonic device performance. The first feature, the QW strain due to a lattice mismatch, is used, along with QW width and composition, for bandgap engineering. The second feature, stacking multiple QWs (MQW), is used to obtain a higher modal gain when compared to a SQW [13].

As mentioned in Section 1.1, the QW is a layer of narrower bandgap semiconductor material sandwiched between two layers of a wider bandgap semiconductor material. Lattice mismatch limits the choice of materials that can be used to form a QW. The lattice mismatch between the QW and the bulk regions is accommodated elastically by the strain in the grown QW as long as its thickness is below some critical value, at which the misfit strain can no longer be accommodated without the misfit dislocation. A misfit dislocation in the QW may result in localized energy states within a bandgap, serving as traps and recombination centers and resulting in poor electrical and optical crystal properties [14]. The effect of the strain on the QW bandstructure, optical and electrical properties was extensively studied in early 1980s [15]. It was found that the strain can be used as another tool to perform the bandgap engineering as shown in Figure 1-4 [16] on the example of the InGaAs/InP QW.

At 53% indium composition, InGaAs QW is lattice matched to the InP substrate and light hole and heavy hole bands are degenerate at the valence band maxima. Bulk InGaAs bandgap decreases with increasing indium composition. In a QW however, a greater than 53% composition of indium results in a compressive strain and an increased bandgap, while a lower than 53% composition produces a tensile strain and a reduced bandgap. The critical thickness of a strained QW can be found theoretically using the mechanical equilibrium model of Matthews and Blakeslee [17], and is confirmed to play an important role in the degradation of the strained QW laser performance [18]. Overall, strained QW lasers benefit from a lower threshold current, higher differential gain and efficiency, and, given the proper parameter matrix, an increased emission spectrum and reliability [19].

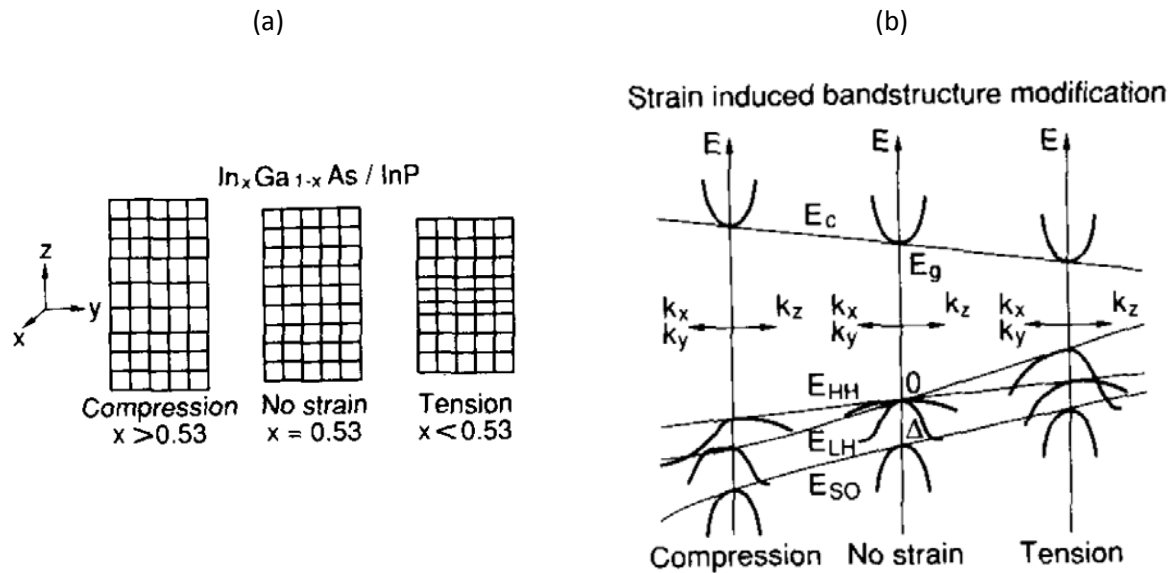


Figure 1-4. Schematic of (a) InGaAs layer with different In composition enclosed in InP and (b) bandstructure modification due to strain in InGaAs layer [16].

The MQW structure was first suggested by R. Dingle and C. H. Henry in 1976 [20] and used to improve a laser diode performance. As the name suggests, the structure is formed by several QWs separated by barriers. Such a design reduces the probability of the wave function

to penetrate from one QW to another. Kurobe et al. [13] studied QW lasers and showed that the modal gain in MQW lasers does not saturate as fast as in SQW (Figure 1-5) allowing for a higher output power.

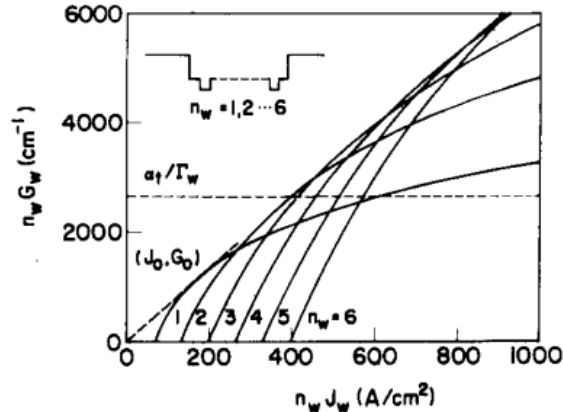


Figure 1-5. Gain ($n_w G_w$) vs. total injected current density ($n_w J_w$) for various numbers of QW n_w . G_w and J_w are the gain and the current density per well respectively [13].

The MQW structure has advantages as well as disadvantages when compared to the single QW (SQW). Unfortunately, a higher number of wells requires higher threshold current density; however, it also offers a higher modal gain when compared to the SQW [21]. While originally used in lasers, the MQW structure found its application in other photonic devices such as photodetectors and modulators. In modulators, the MQW structure allows for high-speed operation at low driving voltages due to a higher electroabsorption effect [22].

A crucial step in developing the optical fiber network is component integration. External modulators have been shown to have low driving voltages and a large modulation bandwidth at 10 Gbit/s [23], [24]. The signal produced by the laser diode needs to be coupled into the modulator with the lowest possible loss. Such coupling requires submicron alignment tolerances [25] and large optical elements [26], which leads to costly packaging. Even carefully coupled external modulators typically have greater than 3 dB insertion loss [26].

Photonic integrated circuits (PICs) have been identified as a key implementation for future advances in optical fiber communication networks due to their lower operating power and higher channel capacity [27]. Several approaches have been offered to manufacture the PIC: evanescent wave coupling [28], butt-joint coupling using the etch-and-regrowth process [29], [30], [31], and selective area growth (SAG) [26], [32], [33], [34]. Among all these techniques, the SAG process is the best at satisfying tight fabrication tolerance and it can be used for large-scale integration [35]. It is also actively used to produce buried heterostructure (BH) QW lasers [36], [37]. A particular advantage of the SAG over the etch-and-regrowth approach is the absence of the etch-related damage, which is known to compromise the quality of the crystal [19]. In this thesis, we will focus on SAG. The next chapter covers the details of SAG including the growth materials, equipment, and conditions.

2. SELECTIVE AREA GROWTH (SAG)

SAG, sometimes also called selective area epitaxy, is an epitaxial layer growth method using a dielectric mask to promote growth in defined areas on a substrate [38]. Substrates for III-V photonic devices traditionally include InP and GaAs. The mask is often made from silicon dioxide (SiO_2) or silicon nitride (Si_3N_4) and can be patterned using conventional photolithography methods. A number of variables such as source type, temperature, pressure, flow rate, III/V ratio, surface crystallographic indices, and mask geometry affect the growth [34], [39], [40], [41], [42] and are rigorously selected and controlled throughout the process. Several SAG growth methods have been developed, but the two most commonly used are metalorganic chemical vapor deposition (MOCVD) and metalorganic molecular beam epitaxy (MOMBE) [41]. This chapter describes mathematical model and processing steps of the SAG methods using III-V compounds as examples.

2.1 SAG Using Metalorganic Chemical Vapor Deposition (MOCVD)

MOCVD is a vapor-phase thin-film crystal growth process, which uses metal alkyls and hydrates as source materials [43]. This method was originally suggested by H. M. Manasevit in 1968 to grow III-V compounds on dielectrics like sapphire and beryllium oxide for microwave devices and lasers [44]. In later years, dielectric substrates were replaced by III-V substrates like InP and GaAs providing better lattice constant match for grown layers. Another modification of MOCVD was the reduction of the reactor pressure from 760 Torr (atmospheric pressure or APMOCVD) to a few mTorr (low pressure or LPMOCVD). Since the growth pressure does not affect the selectivity, both the APMOCVD and LPMOCVD SAG utilize the same growth model. In this thesis, both types of growth will be referred to as MOCVD.

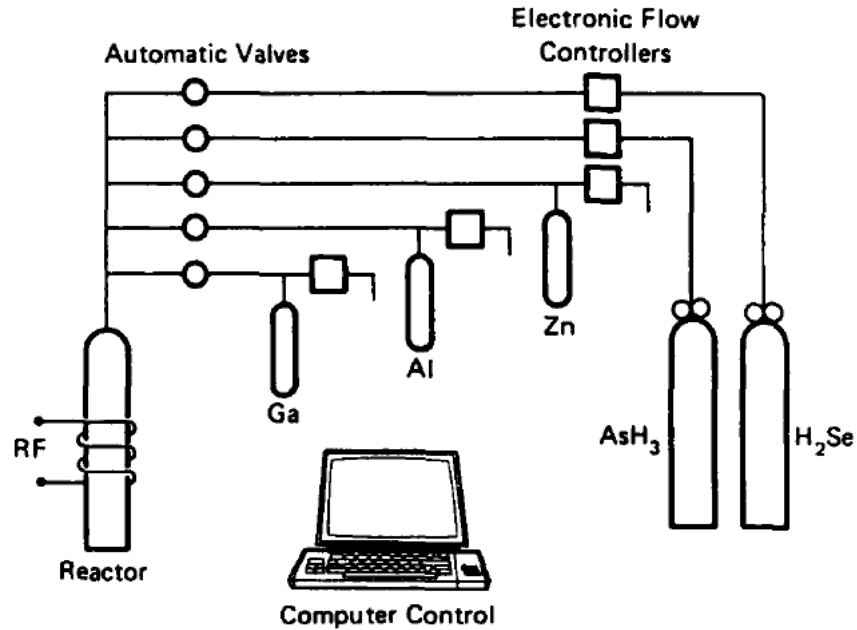


Figure 2-1. Schematic diagram of atmospheric pressure MOCVD reactor [45].

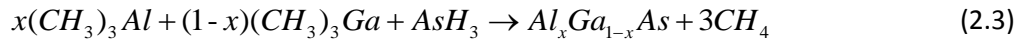
An MOCVD reactor is shown schematically in Figure 2-1 [45] and includes a source system, gas mixing manifold, reaction chamber, and an exhaust system. The source material is picked up in the bubbler by the ultrapure carrier gas (most often a hydrogen), mixed with other sources in the manifold, and delivered to the reaction chamber. Appropriate temperature and material supply inside the chamber facilitate a chemical reaction at a substrate surface, where epilayers are grown. To provide higher uniformity, the susceptor holding a substrate is rotated at some constant speed. While Figure 2-1 shows a vertically oriented reactor chamber, the horizontal orientation is also used. The MOCVD apparatus and its operating principles have been described in detail by Miller and Coleman [45]. The general form of a chemical reaction at a substrate surface can be described as:



where R is some organic, typically an ethyl or methyl, radical, M and Y are some elemental metals, e. g. gallium and arsenic, and n is an integer. One example of such a reaction is GaAs crystal growth:



High purity alkyl sources like trimethylgallium (TMGa), trimethylindium (TMIn), trimethylaluminum (TMAI) and their ethyl analogues are widely used today. Ternary compounds can be formed by adding a third component to the reaction:



As mentioned in Chapter 1, photonic devices based on a ternary compound can be designed to operate at a desired wavelength by choosing the appropriate composition and device structure. The growth profile and composition of III-V compounds depend on multiple growth parameters. By using an effective SAG model, growth results can be predicted based on the appropriate growth parameters.

Predictive growth models of SAG using MOCVD [39], [42], [46], [47] have been developed by several research groups. Since gas flow dynamics and chemical reactions are very complicated, it is customary to simplify the model by only considering the parameters believed to cause the greatest impact.

Surface migration and gas phase diffusion during SAG are the two major growth enhancement processes being widely investigated [41]. Studies of Reep [49] discovered three distinct GaAs growth regimes based on temperature. At low temperatures (<600 °C), morphology of the surface deteriorates due to inefficient pyrolysis of AsH₃. At high

temperatures (>850 °C), growth rate decays due to increased desorption of reactant species from the surface. In the mid-temperature range (600 – 800 °C), growth rate is a linear function of TMGa partial pressure and independent of AsH₃ partial pressure. Thus in the mid-temperature range, growth rate can be conveniently controlled by the supply of group III species. The SAG simulation model presented by Jones and Coleman [39] analyzes a region of the stagnant layer immediately above the surface (Figure 2-2). Assuming SiO₂ stripes dimension to be much longer in z-direction (normal to the paper plane) than in x- or y-direction, we can exclude the z-component from the model due to zero diffusion variation along this direction. The boundary conditions for the simulation cell can be described using Fick's second law, assuming that the reactant's concentration does not change over time:

$$\frac{\partial^2 N}{\partial x^2} + \frac{\partial^2 N}{\partial y^2} = 0 \quad (2.4)$$

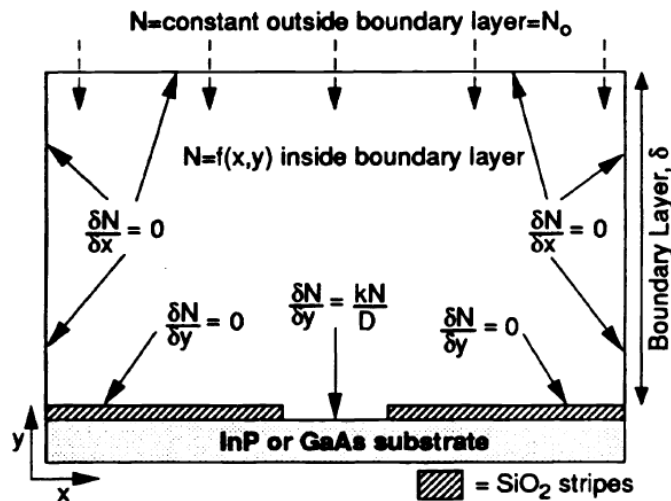


Figure 2-2. Simulation cell schematic for SAG model. N is the concentration of reactants, δ is the layer thickness, D is the effective diffusion coefficient, k is the reaction rate constant [39].

In equation (2.4), N is the concentration of a particular reactant. The reactant gradient at the surface can be described as:

$$\left. \frac{\partial N}{\partial y} \right|_{\text{substrate}} = \frac{k}{D} \cdot N \quad (2.5)$$

$$\left. \frac{\partial N}{\partial y} \right|_{\text{SiO}_2} = 0 \quad (2.6)$$

In equation (2.5), D is the effective diffusion coefficient of group III species, and k is the rate of adsorption of species on the substrate surface per unit concentration. The ratio $\frac{k}{D}$ in (2.5) for elemental materials like indium and gallium can be found empirically from the growth profiles of the corresponding binary compounds InP (InAs) and GaP (GaAs). A boundary layer thickness is related to $\frac{k}{D}$ through the Damköhler number Da , which describes the relative speed of chemical reaction as a function of diffusion [50]:

$$Da = \frac{k\delta}{D} \quad (2.7)$$

Values of D , k and δ in equation (2.7) can be varied by adjusting the growth pressure, temperature, gas flow rate, and the substrate rotation speed.

The reactant is assumed not to adsorb on the masked region. This assumption is valid as long as the growth conditions ensure that no elemental group III species adsorb on the dielectric surface [51]. Upon entering the stagnant layer, the reactant diffuses towards the

unmasked area, where it is consumed. Because of this diffusion, the deposition in the window area immediate to the mask includes a profile effect resulting from reactants, which are not adsorbed on the mask region adjacent to the window [41]. While in some cases this situation is undesirable, certain applications like thickness-modulated waveguide structures [52], and in-plane local bandgap control [53] discussed in Chapter 3 can benefit from it.

The uniformity of grown epilayers can be improved by controlling a vapor phase composition and a source material flow rate [51]. Lowering the pressure of the system increases the species diffusion D just above the substrate. Higher diffusion rate helps to replenish consumed reactant species in the gas phase above the semiconductor at a faster rate, thus improving the uniformity of the vapor composition. Another way to improve the vapor uniformity is to increase the source material flow rate, which effectively decreases δ , until it is significantly higher than the consumption rate of the material at the substrate surface [51].

The effects of mask geometry and its density (ratio of a mask width to a gap width) on SAG have been studied by Gibbon et al. [42]. As shown in Figure 2-3, they use a set of masks with different widths and gap sizes. Mask orientation along a particular crystallographic direction does not change the composition of the epilayers. However, for masks aligned along the $[011]$ orientation an increased defect density is observed when compared to masks aligned to $[0\bar{1}1]$. Darker fields, i.e. samples with higher mask-to-gap width ratio, result in higher indium concentration (Figure 2-3 (a)). The alloy composition shows strong dependence on mask geometry. The studies conducted by Gibbon et al., as well as several other research groups [41], [54], indicate that the gas phase diffusion of a source material is much larger than surface

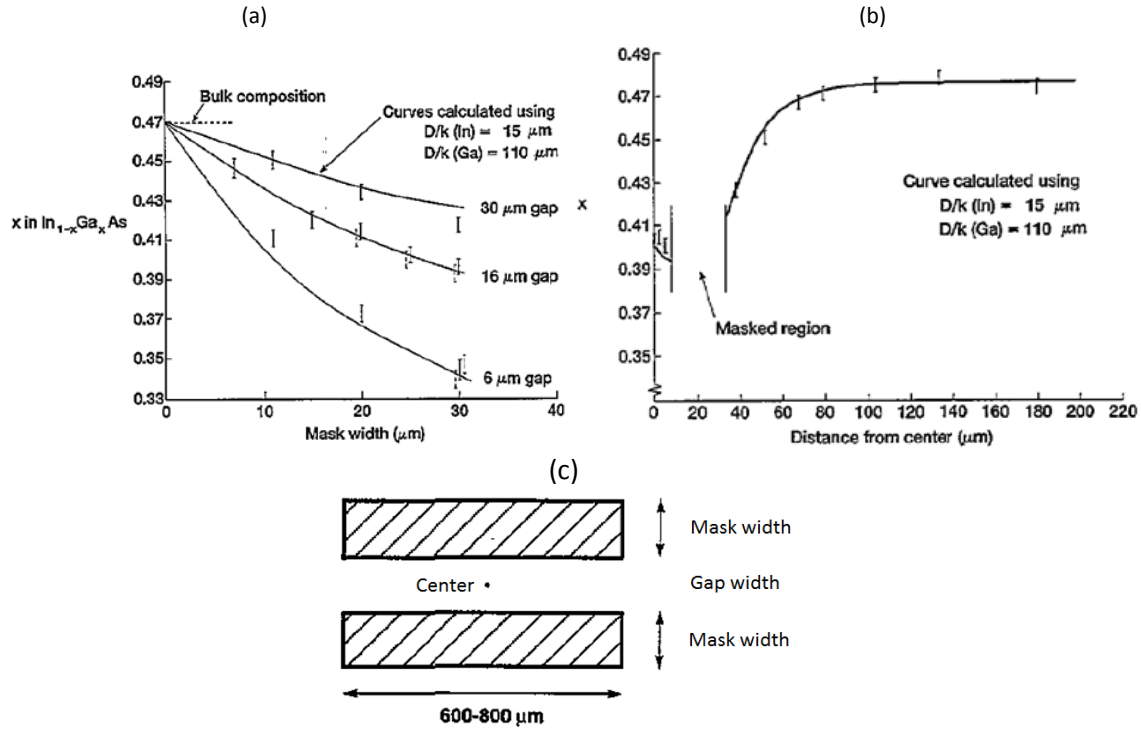


Figure 2-3. (a) Composition of InGaAs at the center of mask window for different mask gaps; (b) Indium composition in InGaAs vs. distance to mask center; (c) Mask design [42].

diffusion in experiments with masks on the order of 10 – 100 μm . Thus, for SAG a mask geometry is as important as growth parameters.

We are now in the position to examine the SAG on a familiar material system and to compare the predicted and experimental results. Consider, for example, growing InGaAs on an InP substrate. The growth rate enhancement E is defined as the ratio of the selective growth rate to the non-selective growth rate. Let x and t be the selective growth composition and thickness, and let x_0 and t_0 be the non-selective growth composition and thickness. The simulation cell is divided into a large number of individual elements, and a finite element method is used to calculate the reactant flux through the layer. A commercially available fluid dynamics analysis software [55] is used by Jones et al. [56] to predict the thickness of selectively grown InGaAs and indium composition:

$$t_{InGaAs} = E_{InGaAs} t_0 = [E_{In} x_0 + E_{Ga} (1 - x_0)] t_0 \quad (2.8)$$

$$x_{In} = \frac{E_{In} x_0}{E_{In} x_0 + E_{Ga} (1 - x_0)} \quad (2.9)$$

This model has been verified by growing InGaAs epilayers on an InP substrate, as shown in Figure 2-4, and measuring the growth profile using the surface profilometer (Figure 2-5) after removing the oxide mask [39].

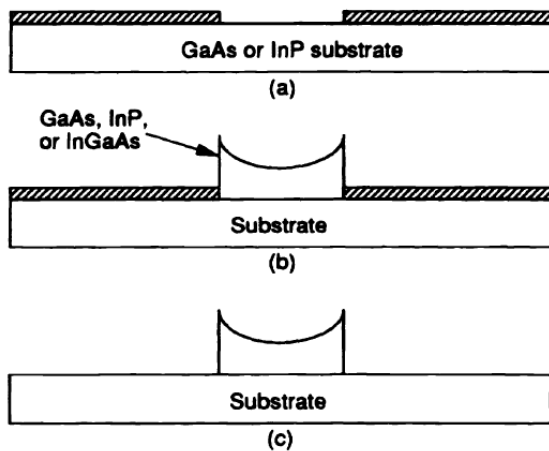


Figure 2-4. Fabrication steps schematic for SAG MOCVD process [39].

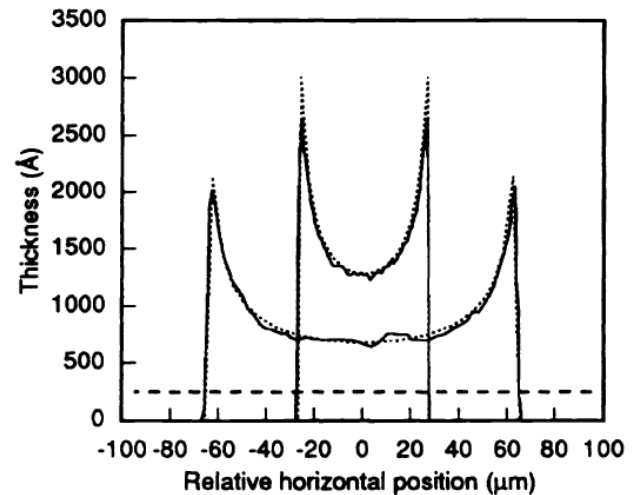


Figure 2-5. Comparing calculated (dotted line) and measured (solid line) growth thickness of 50 μm and 125 μm wide InGaAs windows [39].

Results from both the experiment and the simulation indicate that the growth rate in the middle of the window is significantly lower than that near the mask edges for wide stripe openings. It has also been found that selectively grown indium alloys have higher indium concentration closer to the mask edges [57]. TMI_n is found to decompose at lower temperatures than TMGa and its decomposition products have higher diffusion coefficients than those of TMGa [54], [58], [59]. These findings led to a conclusion that a local growth rate of indium alloy strongly depends on indium concentration in the gas phase above the substrate surface.

This SAG model is based on several important assumptions. First, the mask alignment with respect to the crystallographic axis of the substrate does not affect the epitaxy. Second, the mask dimension in the z-direction (Figure 2-2) is considered infinite when compared to the other two dimensions. Third, the simulation cell is small, so that the diffusion coefficient and the temperature are considered constant. And last, the adsorption rate of the species is proportional to the species concentration just above the surface.

Although the MOCVD SAG model is based on a relatively simple mask design, it can be adapted to accommodate for more complicated designs, allowing bandgap variations within the structure. Shioda et al. [48] studied the mask design shown in Figure 2-6. Photoluminescence of the grown structures (barrier, QW, MQW) was measured along the centerline. Surface diffusion near the mask, ignored in the model, becomes more pronounced for narrow stripes, resulting in deviation between the measured thickness and the calculated one, which, in turn, affected the bandgap calculation (Figure 2-6 (b)). Thus, it can be concluded that the edge growth is greatly influenced by the surface diffusion of species. The associated model has been developed and confirmed by Greenspan et al. [60]. Since the bandgap depends on the mask design, growth parameters have to be carefully considered for each individual structure.

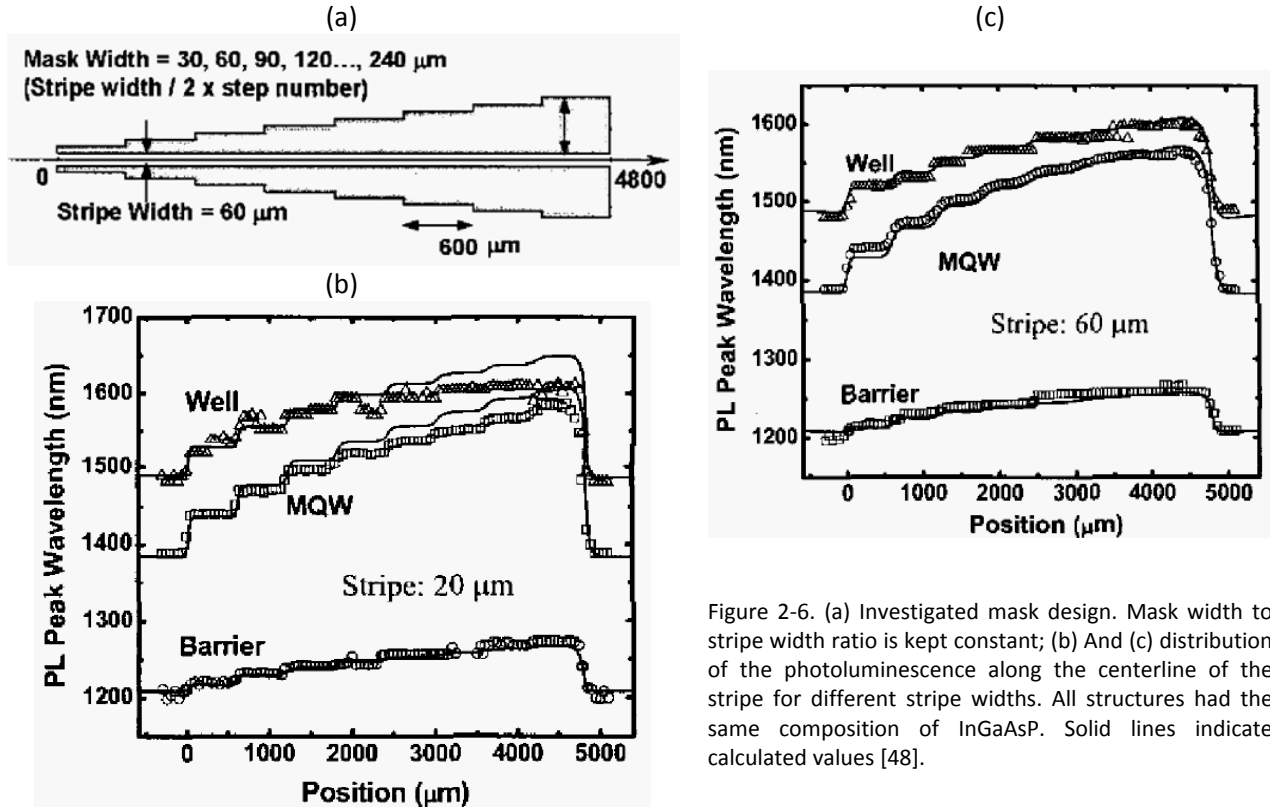


Figure 2-6. (a) Investigated mask design. Mask width to stripe width ratio is kept constant; (b) And (c) distribution of the photoluminescence along the centerline of the stripe for different stripe widths. All structures had the same composition of InGaAsP. Solid lines indicate calculated values [48].

In Section 2.2, we will look at another method of performing SAG and compare its properties with those of MOCVD.

2.2 Molecular Beam Epitaxy (MBE)

The MBE, just like MOCVD, was developed in the late 1960s targeting improvements in epitaxial material deposition. From the schematic of MBE shown in Figure 2-7 [61], one could immediately notice the high complexity level of the system. Some of the main differences from MOCVD include an ultra-high vacuum operation, the need for cryogenic cooling, and an ability to perform in situ examination of the sample.

In situ analytical tools are a potential advantage of MBE, because they provide real-time information on growth mechanisms, uniformity, and stoichiometry [45]. These tools include reflection high-energy electron diffraction (RHEED), Auger spectrometry and

ellipsometry for surface analysis, and mass spectrometry for residual background partial pressure analysis [61]. Note that many of these are not available during actual layer growth.

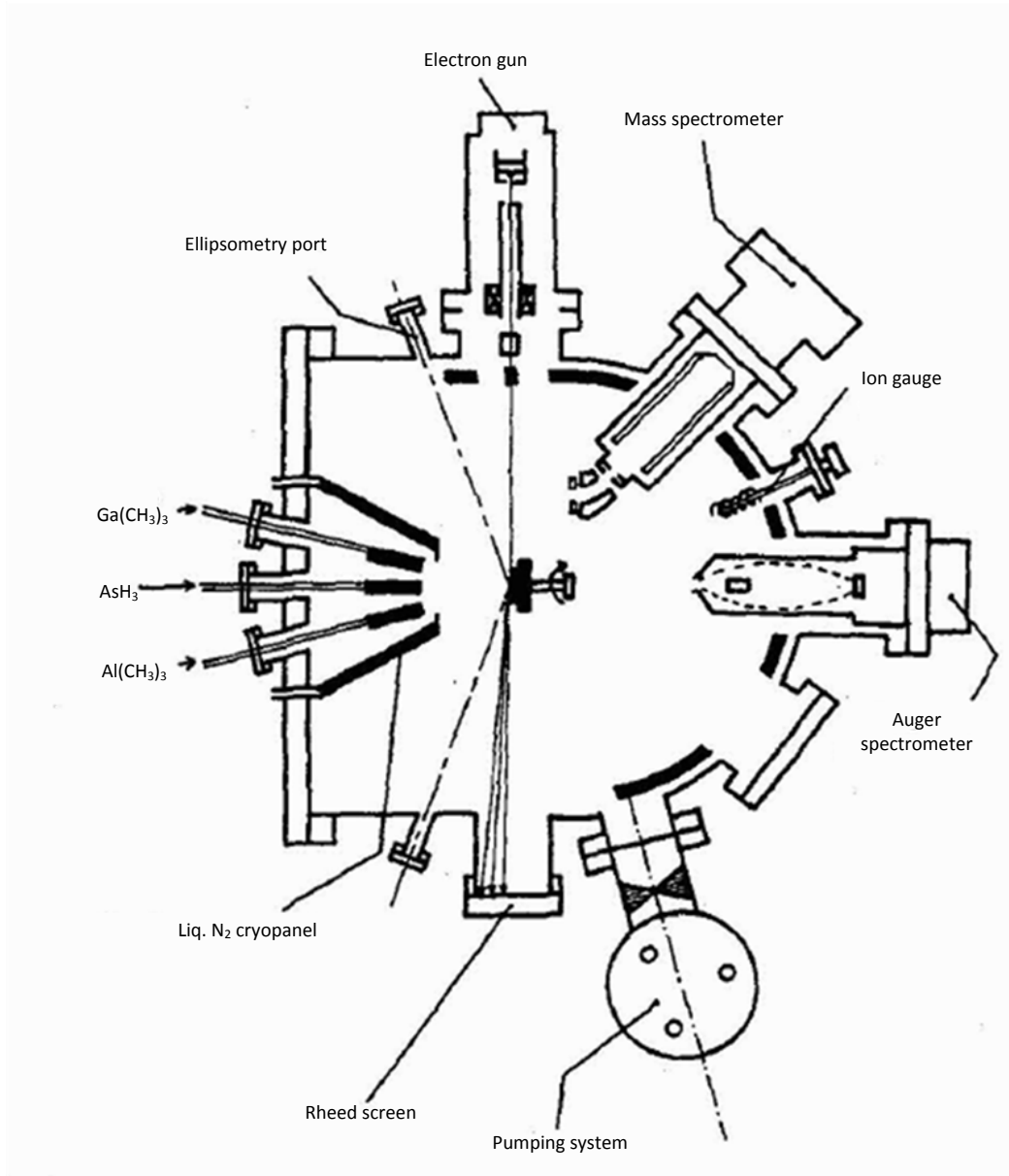


Figure 2-7. Metalorganic MBE schematic [61].

The ultra-high vacuum inside the chamber increases the mean free path of the elemental source molecules to ensure their delivery to the growth substrate. Using elemental sources in MBE eliminates the carbon contamination, which is often a problem for MOCVD.

Solid MBE sources like gallium and indium are heated in the effusion cell until they start to sublime. Source species in the gaseous phase then exit the effusion cell and adsorb and diffuse on the heated substrate. True selectivity using the elemental sources MBE under particular conditions has been demonstrated on GaAs [62]. However, the difficulties arise with the selective growth of ternary and quaternary compounds.

Raising the substrate temperature while growing ternary and quaternary compounds leads to increased re-evaporation of the material from the surface [63]. If we try to compensate for this phenomenon by increasing the source flow rates, we lose the selectivity property. The control of the sources' flow rate proves to be very difficult because of this situation. The suggested solution for this problem is to switch to a different type of source material [64], [65].

An MBE apparatus can be modified to use metal alkyls (group III) and gaseous hydrates (group IV) sources instead of elemental ones. A system modified this way is called metalorganic MBE (MOMBE) and uses electronic mass-flow controllers to adjust the flows of particular sources. The cryogenic cooling of the elemental species shown in Figure 2-7 is required to capture the water vapor and the carbon hydrates and prevent sample contamination. We will focus our attention on ternary and quaternary compounds and respective metalorganic sources used in MOMBE.

The major MOCVD SAG growth parameters have been discussed in Section 2.1. MOMBE SAG also depends on those parameters (Figure 2-8 [41]). The biggest observable difference between the two growth methods is the effect of III/V ratio on SAG. As the graphs indicate, MOCVD is immune to changes in III/V partial pressure ratio, which is not true for

MOMBE. It has been suggested by Kayser [41] that a group V elemental material, obtained by cracking a respective hydrate in the effusion cell, serves as a catalyst for a group III material deposition.

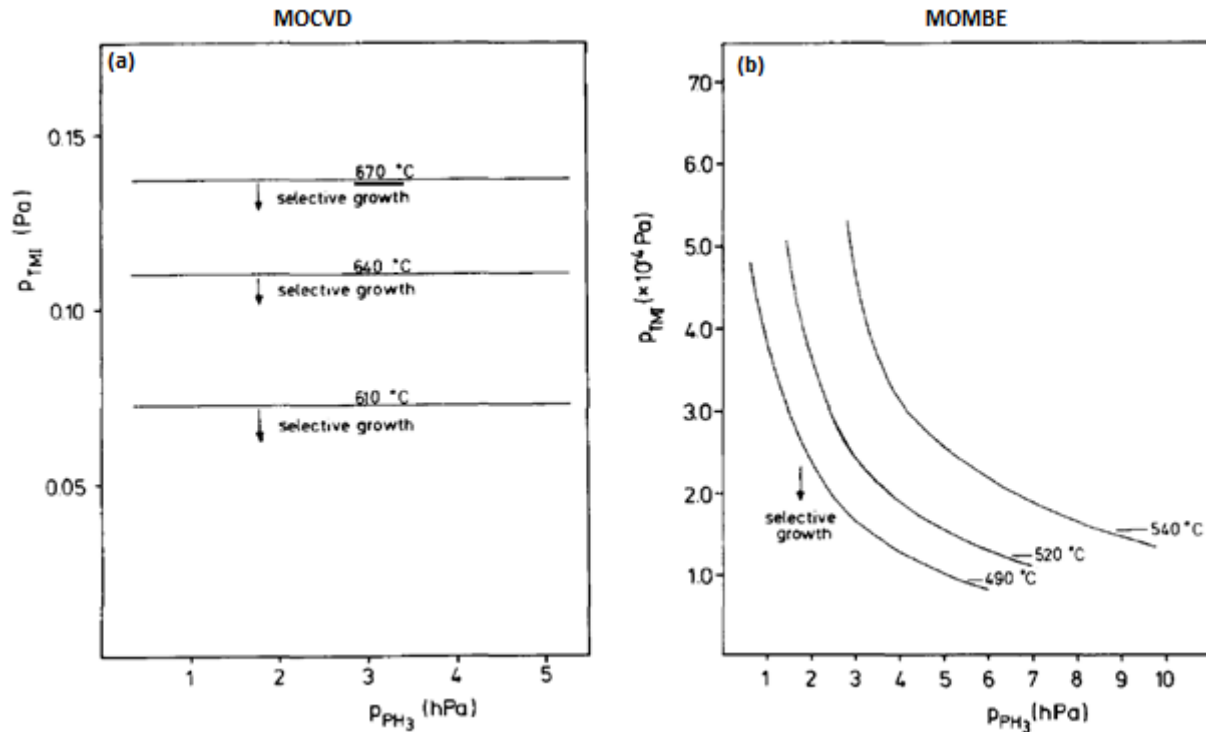


Figure 2-8. Conditions for selective area growth in MOCVD vs. MOMBE. Lines are separating regions with selective growth mode from non-selective [41].

Facets of a structure grown in an un-masked region using MOMBE and MOCVD will see different growth rates depending on the supply rate of the source material (Figure 2-9) [41]. Species adsorbed on the slow growth rate surface (111)B will migrate to the higher growth rate surface (100) given that the migration length exceeds the length of the facet. At a low III/V ratio this migration length is too short for a significant migration to happen in MOCVD as shown in the middle schematic of the figure. In MOMBE, a limited migration along (100) surface is observed for a high flow rate of group V species.

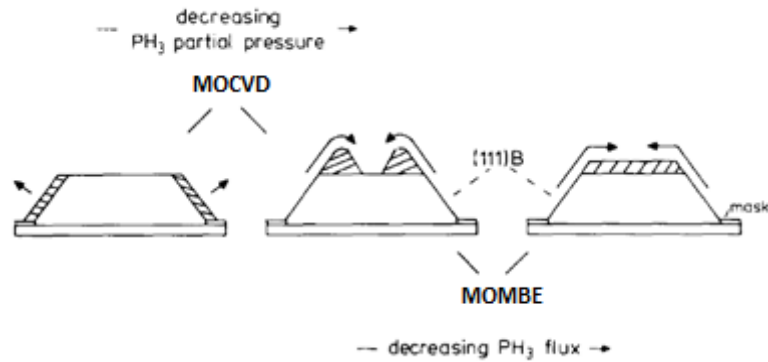


Figure 2-9. Surface migration on (111)B and (100) as a function of PH_3 supply for MOMBE and MOCVD [41].

It is shown in Section 2.1 that the composition of the epilayers grown by MOCVD strongly depends on the proximity of mask edges. Gas phase diffusion is responsible for growth rate enhancement in regions adjacent to mask edges. In MOMBE, gas phase interactions between the species are not present, thus the epilayer composition and thickness are independent of the mask geometry and proximity [66]. This can be viewed as an advantage of MOMBE in manufacturing of the integrated photonic devices, since the mask design does not pose any restrictions on the epitaxial structure design [34].

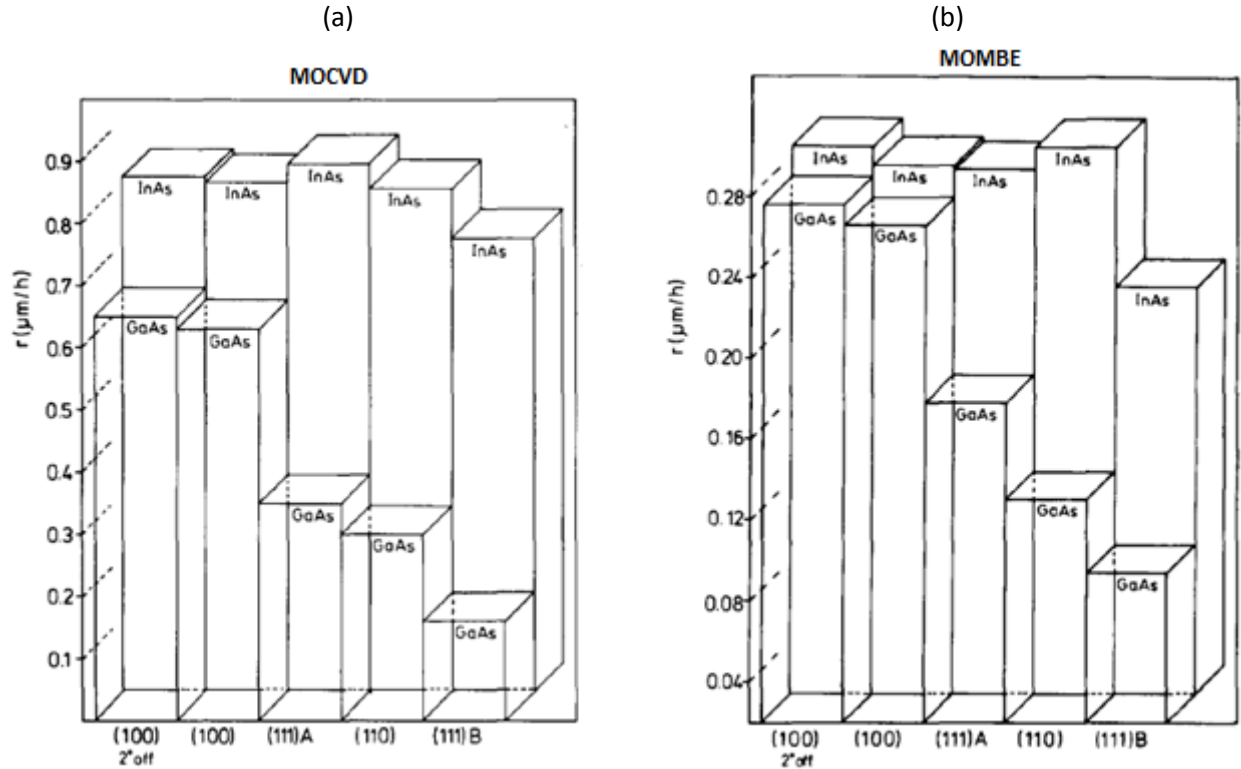


Figure 2-10. InGaAs growth rate in terms of growth rates of GaAs and InAs for (a) MOCVD and (b) MOMBE [41].

The reaction coefficients and the migration lengths of individual elements during SAG are investigated next. The easiest way to do that is to perform the non-selective growth of the ternary compound (InGaAs) and to express its growth rate in terms of the binary compounds (InAs and GaAs) growth rates (Figure 2-10 [41]). Such experiments have been performed using MOCVD and MOMBE on substrates with several different crystallographic orientations. The results for (111)A and (110) oriented substrates suggest that the growth rate and the composition of the ternary compound is determined by the slowest adsorbing (GaAs) constituent for both the MOCVD and MOMBE. A peculiar difference between the two methods is observed for the case of (111)B orientation. Much lower growth rate for MOMBE in this direction is a result of the indium precursor saturation, which can be explained by the surface kinetic limitations for this reaction [41].

This chapter reviewed the two major SAG techniques, which can be used in III-V device manufacturing. Chapter 3 will discuss how the SAG methods can be used to manufacture integrated photonic devices for telecommunication.

3. SELECTIVELY GROWN PHOTONIC QW DEVICES

As mentioned in Chapter 1, advancements in MOCVD and MBE have made it possible to manufacture high quality QW structure. Photonic devices based on this structure benefit from a number of enhanced properties also described in Chapter 1. Devices grown simultaneously on the same substrate are easier to integrate with each other, improving, for example, the coupling efficiency between the light source and modulator. An example of simultaneously grown QWs with different bandgaps using the SAG model was shown in Figure 2-6. This chapter will focus on the applications of selectively grown QW structures in lasers and modulators.

3.1 QW Laser

3.1.1 Theory of QW Laser

From the p-n junction to the double heterostructure to the QW laser, the performance of light-emitting devices has improved over time. QW lasers are known for their low threshold current density [67], [68], lasing wavelength tunability [69], and low temperature dependence

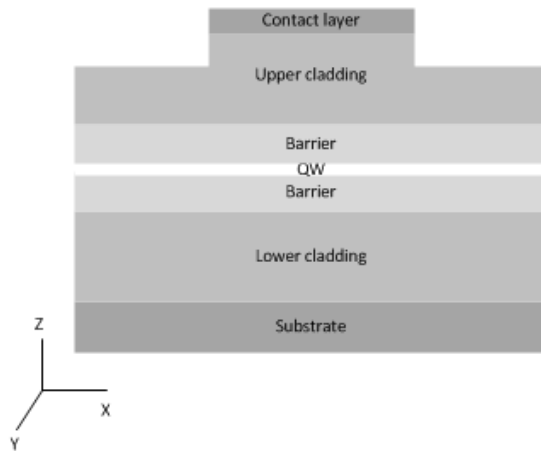


Figure 3-1. QW laser schematic cross section.

of the threshold current [70]. A typical QW laser includes the active, the barrier, the cladding, and the contact layers grown on a substrate, as shown schematically in Figure 3-1. By choosing the appropriate material composition for those layers, we create a potential barrier for the carriers trapped within the QW. Such quantum confinement enhances the carrier recombination probability within the QW. The cavity is created along the y -direction by cleaving the front and rear facets. A multiple QW (MQW) laser follows the same design, replacing a single QW with several QWs separated by the barriers, which reduces the wavefunction coupling between the wells. One of the fundamental merits of a QW is the density of states (DOS), ρ , which for electrons in the conduction band is found as

$$\rho_c(E) = \sum_{n=1}^{\infty} \frac{m_c}{\pi\hbar^2} H[E - \varepsilon_n] \quad (3.1)$$

where $H[x]$ is the Heaviside function, m_c is the electron effective mass, ε_n is the quantized energy level of the electrons in the n^{th} subband. If the potential barrier can be considered infinitely high, ε_n is found as

$$\varepsilon_n = \frac{(n\pi\hbar)^2}{2m_c L_z^2} \quad (3.2)$$

where L_z is the well thickness. The DOS of an MQW structure can be found using Eq. (3.1) by multiplying the RHS by the number of wells. In practice, the potential barrier height is finite. Therefore, if the barrier between the wells is not thick enough, strong coupling may arise and result in splitting of the energy levels further within each well. The corresponding DOS can then be found as

$$\rho_c(E) = \sum_{n=1}^{\infty} \sum_{k=1}^N \frac{m_c}{\pi \hbar^2} H[E - \varepsilon_{nk}] \quad (3.3)$$

where N is the number of wells. Thus, a strong coupling within an MQW structure of a laser results in the emission spectrum broadening and is usually undesirable. The major advantage of an MQW laser over an SQW laser is its higher modal gain (Figure 3-2) that has been predicted and confirmed experimentally [10]. However, higher modal gain requires higher threshold current density, thus introducing a tradeoff.

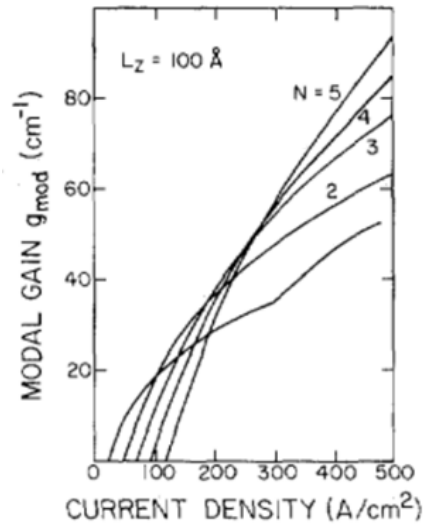


Figure 3-2. The modal gain as a function of the injected current density for various number of QW (N) [10].

Advantages of QW lasers are based on carrier confinement in the active region. Additional modifications of a QW laser structure have been suggested to get even higher performance. A buried heterostructure laser discussed in the next section provides both electrical and optical mode confinement in the transverse as well as lateral dimensions.

3.1.2 Buried Heterostructure (BH) Laser

A BH laser provides improved electrical and optical confinement simultaneously [71] when compared to a regular QW laser. Since the active region material, AlGaAs, immediately oxidizes when exposed to the air, a conventional growth and etch technique cannot be used.

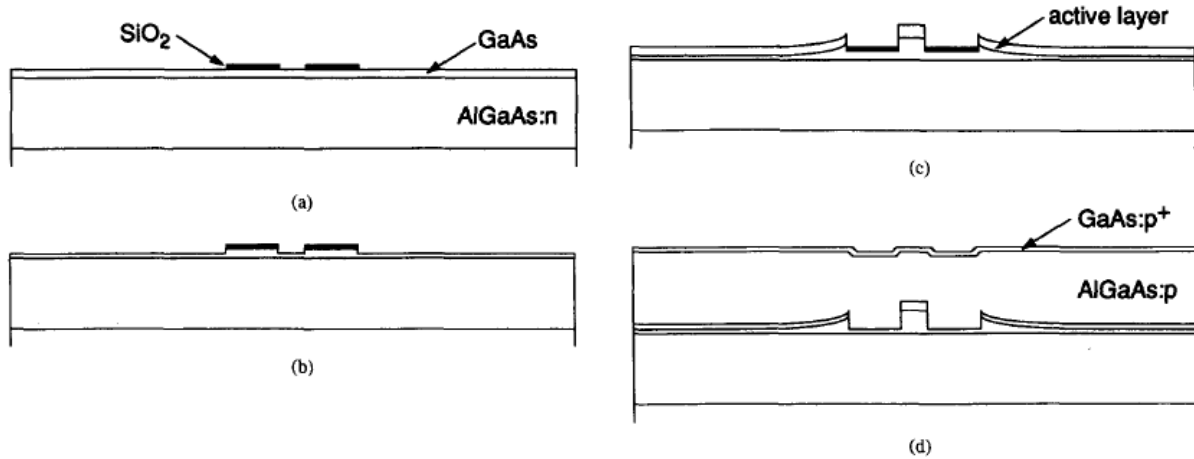


Figure 3-3. Three-step growth sequence used to fabricate the BH lasers. (a) Growth of GaAs buffer layer, AlGaAs lower confining layer and GaAs electrical confining layer. Dielectric strips are separated by 4 μm; (b) Result of etch step to remove processing damage; (c) Selective growth of the GaAs-InGaAs active region mesa; (d) Growth of the AlGaAs upper confining/burying layer [19].

Instead, a three-step growth process for a BH using MOCVD SAG has been developed as shown in Figure 3-3 [19]. A mask composed of two SiO₂ stripes is used to define an active region. According to the model from Section 2.1, growth rate and material composition in the active region can be varied by adjusting the stripe width (Figure 3-3 (c)). The active region composition, in turn, affects the emission wavelength of a laser. Figure 3-4 (a) adapted from [19] shows the emission wavelength dependence on the oxide stripe width. This structure, however, has some disadvantages. Because of the large index difference in the lateral direction (Figure 3-4 (b)), higher order modes will be supported, which calls for beam instability [72].

Ridge waveguide structure is often used for optical mode guiding as a way to separate the electrical and optical confinement within laser structure.

A RW structure (Figure 3-5 (a)) enables high power single-mode lasing as demonstrated by Huber et al. in [73]. A flared waveguide tapered along the length of a laser grown using SAG provides a high gain volume (Figure 3-5 (b)). The geometry of the waveguide suppresses higher order optical modes and allows for a smaller index step when compared to BH laser.

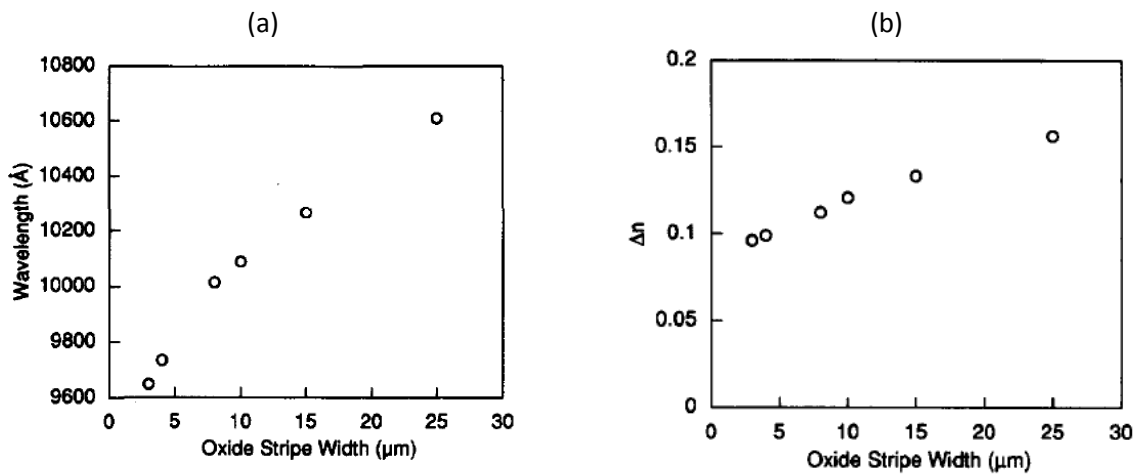


Figure 3-4. (a) BH laser wavelength dependence on the oxide stripe width; (b) Refractive index step between the active region and the lateral confinement layer [19].

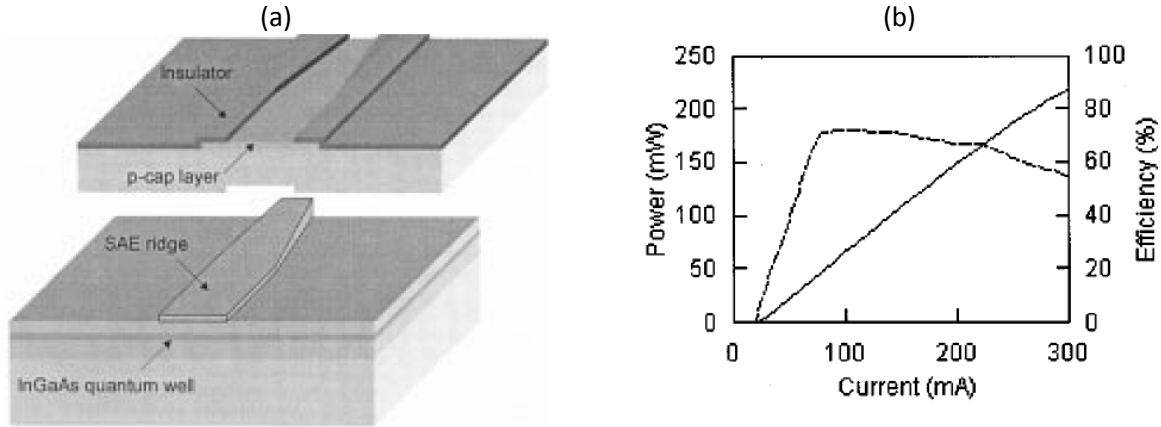


Figure 3-5. (a) Schematic of laser structure before contacts deposition. The upper cladding layers have been displaced to reveal the flared and tapered waveguide layer; (b) Power (solid line) and differential quantum efficiency (dashed line) vs. current for flared tapered laser [73].

Combining the RW and BH techniques in laser manufacturing has been demonstrated by Swint et al. [12]. They called their structure a separate lateral confinement (SLC) QW laser, since the electrical carriers and photons are not confined in the same region. An SLC laser can be manufactured using a BH laser manufacturing steps followed by the ridge etching. This structure inherits the low threshold current benefit of a BH and the enhanced optical guiding properties of a RW laser. Separation of the optical and electrical confinement presents the ability to control each one independently.

This section briefly reviewed the theory of a fundamental QW laser and several improved designs offered by the SAG technique. Section 3.2 will discuss laser light modulation using an electro-absorption modulator.

3.2 Electro-Absorption Modulator (EAM)

In general, optical modulation can be performed by tuning the amplitude, frequency, phase, or polarization of the beam via varying certain properties of the propagation material. The EAM is an electrically controlled optical component that is made from semiconductor

material and modulates the amplitude of the laser beam. Although beam modulation can be performed directly by modulating the driving current of a laser, a dynamic line broadening will be observed at high frequency due to chirping [74]. Modulation of the driving current causes carrier density variation within the active region. Such variation results in frequency chirping, which can affect signal detection on the receiver end of the system. EAM operation is based on a different effect, which allows for much higher operating frequency. We will focus on III-V EAMs since they can be fabricated on the same substrate as the lasers discussed in Section 3.1.

The absorption spectrum of EAM can be controlled by applying an external electric field across its active region. This phenomenon is called the Franz-Keldysh effect and was observed in EAMs with a bulk semiconductor active region in the late 1950s [75]. An applied electrical field can also affect the light polarization inside a semiconductor material as described by the Pockel's effect [76]. The absorption spectrum in a bulk semiconductor EAM is a continuous function, while in a QW based EAM, this function displays a stepwise behavior based on the DOS as described by Miller et al. in [77]. A stepwise behavior of the absorption spectrum is preferred over the continuous one, since it can provide greater intensity change per unit change of an applied field. Modulation enhancement in a QW EAM is explained by the quantum-confined Stark effect (QCSE). In addition to the absorption spectrum change, the exciton binding energy in a QW is also increased, which results in clear exciton resonances in GaAs-AlGaAs QWs at room temperature [78], [79]. Miller suggests several mechanisms responsible for such behavior. First, the electric field applied perpendicular to the QW layers pulls the electrons and holes toward the opposite sides of the layers, thus reducing the Coulomb force. Second, the separation of carriers is limited by the well walls. Third, the

electron-hole interaction, although weakened by the separation within the QW (~ 10 nm), is still strong, since the exciton size is ~ 30 nm. Thus, the exciton resonance in QW can sustain much higher fields than in the bulk and result in larger absorption shifts without significant broadening.

A typical schematic of an EAM, in which an electric field and an incoming beam are coaligned, is shown in Figure 3-6 [80]. In general, an incoming beam can be set either perpendicular to or parallel to the QW plane. Although a laser-modulator system with an external EAM offers higher modulation frequency when compared to direct laser modulation, such a system suffers from high insertion loss, intracavity reflection, and the need for bulky and expensive coupling optics [39]. These problems are addressed by integrating the EAM and the laser on the same substrate as discussed in the next section.

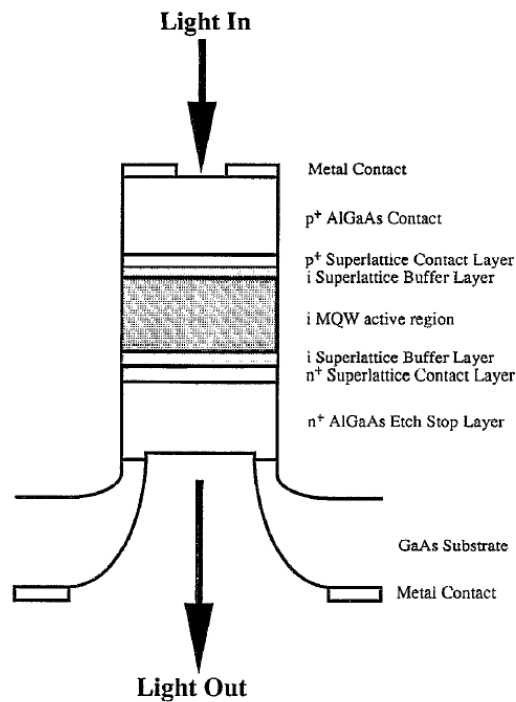


Figure 3-6. Schematic of EAM [80].

3.3 Integrating a QW Laser and EAM

Integration of a laser with an EAM has been made possible because of the ability to control the in-plane bandgap energy during SAG as explained in Chapter 2. Using such integrated structure, transmission rates over 10 Gb/s were reported in the early 1990s [81]. Significant research effort in subsequent years [35], [53], [82], [83] helped to improve the operating properties of the laser and modulator, making 10 Gb/s links a standard of optical fiber communication.

A schematic of an MQW distributed Bragg reflector (DBR) laser integrated with an EAM using selective area MOCVD is shown in Figure 3-7 (a) [36]. In Figure 3-7 (b), the width of the dual oxide stripes changes from 16 μm in the laser section to 12 μm in the modulator section, with spacing between the stripes maintained at 4 μm . According to SAG model from Chapter 2, different stripe widths result in different compositions of the laser and modulator active regions. The emission and the absorption wavelengths are $\lambda_{\text{LD}}=1.026 \mu\text{m}$ and $\lambda_{\text{M}}=0.999 \mu\text{m}$, respectively. Theoretically, photonic devices with absorption/emission spectra between 960 nm and 1060 nm can be grown on the same substrate simultaneously. In this experiment, the oxide stripes are longer in the laser region (700 μm), where the enhanced growth rates are higher than those in the modulator region (490 μm). The three-dimensional SAG model is used to determine the best location for the 100 μm long DBR grating. At a distance 150 μm away from the change of the oxide stripes width, the active region thickness variation is 0.62% across 100 μm . Placing the DBR grating any closer to the laser region would result in chirped gratings due

to higher active region thickness variation. An additional 7 nm range of wavelength tunability is achieved by injecting a current through the DBR contact and inducing a carrier heating.

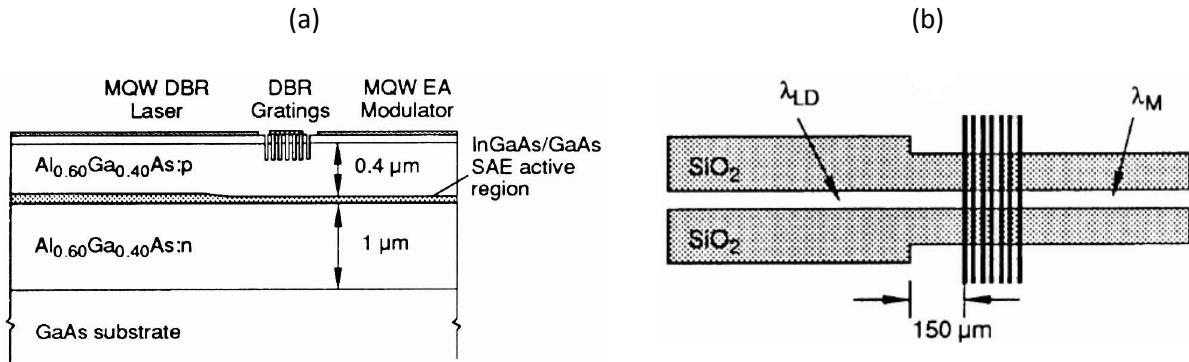


Figure 3-7. (a) Schematic diagram of a DBR laser with an integrated EAM; (b) Schematic diagram of the growth mask used for the active region regrowth [36].

Although the IEEE standard 802.3ae-2002 supporting 10 Gb/s transmission rates was released in 2002, chirp and bias voltage [84] as well as thermal stability [85] of EAM are being constantly improved. At the same time MOCVD grown MQW EAMs are pushed to operate at 20 and even 40 Gb/s transmission rates by introducing improved optical coupling sections, switching from a conventional QW to a shallow QW structure, and several other modifications [86], [87], [88].

4. CONCLUSION AND FUTURE PERSPECTIVES

QW photonic devices have become standard components of optical fiber communication systems, allowing for transmission rates in excess of 10 Gb/s. The operation of these devices is based on discretely separated energy levels as a result of 1 dimensional confinement of carriers within a QW. Discrete energy levels provide an abrupt stepwise discontinuity in the absorption and the emission spectra of QW modulators and lasers. These and other benefits of a QW structure were described in Chapter 1. It became possible to manufacture a QW structure after the epitaxial growth techniques like MOCVD and MBE had been developed in the 1960s. These techniques have their own advantages and disadvantages, and both of them allow precise control of the growth conditions. The substrate and the growth materials are often chosen from III-V alloys with a direct bandgap in the desired near-IR region. Major growth mechanisms of MOCVD and MBE are reviewed in Chapter 2. A mathematical growth model was introduced and used to design and fabricate integrated photonic devices.

A communication system where a laser and an external EAM are respectively used as the light source and the modulator significantly outperforms a copper wire network. The optical communication system has higher channel capacity and extremely low crosstalk, and is immune to EM noise as mentioned in Chapter 1. The SAG technology can further improve such optical system performance by integrating the laser and EAM using the model reviewed in Chapter 2. Such integration is possible because SAG is capable of designing the in-plane bandgap variation, i.e. the ability to simultaneously grow devices with different energy transition levels on the same substrate. While SAG mechanisms are not yet fully understood, the mathematical model of SAG for III-V alloys shows a good correlation with the experimental results. Chapter 3 gave

the examples of a selectively grown buried heterostructure laser and a laser integrated with a modulator.

The two-dimensional SAG model for vapor phase diffusion is constantly being revised and updated using different approaches. In 2008, Dupuis et al. [89] compared the finite differences, finite elements, and the fast Fourier transform methods to solve for the boundary conditions and found their results to be within the error margins of each other. They studied AlGaInAs alloy, which has not received as much attention as the more common GaInAsP. Recently, SAG technology has been widely used to grow group III nitrides (GaN, InGaN, etc) [90], [91] as well as devices based on quantum dots (QDs) [92], [93], [94] based photonic devices in order to investigate their electro-optical properties.

Current research aims to both improve current SAG technology for QW and to adapt it to grow nanostructures with higher confinement factor, which could potentially replace QW in the future.

APPENDIX A – Al_xGa_yIn_{1-x-y}As BANDGAP CALCULATION

Since there is no available model for the bandgap calculation as a function of the composition of a quaternary alloy with three components on the column III sublattice, we use a general formula:

$$E_g(A_xB_yC_{1-x-y}D) = a + bx + cy + dxy + ex^2 + fy^2 + gx^2y + hxy^2 \quad (\text{A.1})$$

The coefficients a through f can be found from the boundary conditions by using a set of combinations of (x, y) , i. e. $(0, 0)$, $(0, 1)$, $(x, 1-x)$, and so on for the right-hand side of (A.1) and equating it to the bandgap of corresponding binary or ternary alloy. For example, if we let (x, y) to be $(0, 0)$, the equation (A.1) becomes:

$$\begin{aligned} E_g(A_0B_0C_1D) &= a + bx + cy + dxy + ex^2 + fy^2 + gx^2y + hxy^2 = a \\ E_g(CD) &= E_g(InAs) = 0.36 \text{ eV} = a \end{aligned}$$

Solving a corresponding system of boundary condition equations yields the following result:

$$a = 0.360, b = 2.093, c = 0.629, d = -0.987, e = 0.577, f = 0.436$$

The coefficients $g = 2$ and $h = 2$ cannot be found this way; instead they are obtained from fitting the theoretical curve to experimental one [95].

The bandgap plot shown in Figure 1-2 has been generated using a Matlab code presented below:

```

clear all;
x=0:0.001:1;          %Al composition
y=0:0.001:1;          %Ga composition
[x,y] = meshgrid(x,y);
z=0.36+0.629.*y+2.093.*x+1.013.*x.*y+0.436.*y.^2+0.577.*x.^2-2.*x.*y.*(1-x-y);
%the bandgap formula
for j=1:1001          %this part of the code ensures x+y<=1 by zeroing out
    for k=1:1001      %all elements with x+y>1 of the bandgap matrix
        if (j+k)>1002
            z(j, k)=0;
        end
    end
end
surf(x,y,z); xlabel('Al'); ylabel('Ga'); zlabel('Eg');
shading flat;

```

APPENDIX B – DENSITY OF STATES

Density of states (DOS) of a material describes the number of states per energy interval per unit volume at a particular energy level, which can be occupied by carriers. This value is one of the key parameters taken into consideration when analyzing material electrical properties. Number of electrons per unit volume in the conduction band is

$$n_c = \sum_{\mathbf{k}} f(E) = \int_{E_c}^{\infty} f(E)g(E)dE \quad (\text{B.1})$$

where $f_n(E)$ is the Fermi-Dirac distribution and $g(E)$ is DOS. We want to find the number of states at energy level E in the interval $[E, E + dE]$. For the purpose of this calculation we assume a spherical surface of the constant energy in the momentum (k) space. The volume of this sphere is $V_k = \frac{4\pi k^3}{3}$. If we further assume parabolic shape of the conduction band, i.e.

$E = E_c + \frac{\hbar^2 k^2}{2m^*}$, where m^* is the effective mass, then the volume of the sphere becomes

$$V_k = \frac{4\pi}{3} \left[\frac{2m^*(E - E_c)}{\hbar^2} \right]^{3/2} \quad (\text{B.2})$$

The volume of a unit cell in that sphere is $dk_x dk_y dk_z = \frac{(2\pi)^3}{L_x L_y L_z} = \left(\frac{2\pi}{L} \right)^3$. Knowing the total

volume of the sphere and unit cell, number of states within the sphere is calculated as

$$N(E)_{3D} = \frac{2V_k}{\left(\frac{2\pi}{L} \right)^3} \quad (\text{B.3})$$

where the factor of 2 is accommodating for the electron spin. The DOS per unit volume at the energy level E is found to be

$$g(E)_{3D} = \frac{1}{L^3} \frac{dN(E)}{dE} = \frac{1}{2\pi^2} \left(\frac{2m^*}{\hbar^2} \right) \sqrt{E - E_c} \quad (\text{B.4})$$

We can use the same analogy to derive 2 dimensional (2D) DOS. Starting with a constant energy circle, whose area in k space is

$$A_k = \pi k^2 = \frac{\pi(E - E_c)2m^*}{\hbar^2} \quad (\text{B.5})$$

and knowing that a single state occupies the area $dk_x dk_y = \frac{(2\pi)^2}{L_x L_y} = \left(\frac{2\pi}{L} \right)^2$, the total number of

states within the circle accounting for the 2 electron spins is calculated as

$$N(E)_{2D} = \frac{2A_k}{\left(\frac{2\pi}{L} \right)^2} \quad (\text{B.6})$$

And 2D DOS is found to be

$$g(E)_{2D} = \frac{1}{L^2} \frac{dN(E)}{dE} = \frac{m^*}{\hbar^2 \pi} \quad (\text{B.7})$$

Thus 2D DOS, unlike the bulk semiconductor DOS, does not show proportional dependence on energy. DOS for 3D and 2D semiconductor structures are sketched in Figure 1-3 (c) according to equations (B.4) and (B.7) respectively.

REFERENCES

- [1] J. Kani and H. Nakamura, "Recent progress and continuing challenges in optical access network technologies," in *2012 IEEE 3rd International Conference on Photonics (ICP)*, 2012, pp. 66–70.
- [2] T. Miya, Y. Terunuma, T. Hosaka, and T. Miyashita, "Ultimate low-loss single-mode fibre at 1.55 μm ," *Electronics Letters*, vol. 15, no. 4, pp. 106–108, 1979.
- [3] R. Craig and B. Gignac, "High-power 980-nm pump lasers," in *Optical Fiber Communications, 1996. OFC '96*, 1996, pp. 228–229.
- [4] K. Thyagarajan and A. Ghatak, "Erbium-doped fiber amplifiers and fiber lasers," in *Fiber Optic Essentials*, Hoboken, NJ, USA: John Wiley & Sons, Inc., 2007.
- [5] T. M. Cockerill, J. Honig, D. V. Forbes, and J. J. Coleman, "Distributed feedback strained layer quantum well heterostructure 980 nm laser fabricated by two-step metalorganic chemical vapor deposition," *Applied Physics Letters*, vol. 62, no. 8, pp. 820–822, Feb. 1993.
- [6] K.-H. Goetz, D. Bimberg, H. Jürgensen, J. Selders, A. V. Solomonov, G. F. Glinskii, and M. Razeghi, "Optical and crystallographic properties and impurity incorporation of $\text{Ga}_{1-x}\text{In}_x\text{As}$ ($0.44 < x < 0.49$) grown by liquid phase epitaxy, vapor phase epitaxy, and metal organic chemical vapor deposition," *Journal of Applied Physics*, vol. 54, no. 8, pp. 4543–4552, Aug. 1983.
- [7] P. J. A. Thijs, L. F. Tiemeijer, J. J. M. Binsma, and T. Van Dongen, "Progress in long-wavelength strained-layer InGaAs(P) quantum-well semiconductor lasers and amplifiers," *IEEE Journal of Quantum Electronics*, vol. 30, no. 2, pp. 477–499, 1994.
- [8] V. Yakovlev, "High performance AlGaAs -based laser diodes: Fabrication, characterisation and applications," presented at the 20th International Conference on Microelectronics, 1995. Proceedings, 1995, vol. 1, pp. 435–439.
- [9] E. Kuphal, "Phase diagrams of InGaAsP , InGaAs and InP lattice-matched to $(100)\text{InP}$," *Journal of Crystal Growth*, vol. 67, no. 3, pp. 441–457, Aug. 1984.
- [10] Y. Arakawa and A. Yariv, "Quantum well lasers-gain, spectra, dynamics," *IEEE Journal of Quantum Electronics*, vol. 22, no. 9, pp. 1887–1899, Sep. 1986.
- [11] V. P. Gupta and N. M. Ravindra, "Comments on the Moss formula," *Physica Status Solidi (b)*, vol. 100, no. 2, pp. 715–719, 1980.
- [12] R. B. Swint, C. Y. Woo, A. E. Huber, S. D. Roh, J. J. Coleman, B. O. Faircloth, and M. S. Zediker, "A novel separate lateral confinement quantum-well heterostructure laser," *IEEE Photonics Technology Letters*, vol. 14, no. 2, pp. 134–136, Feb. 2002.
- [13] A. Kurobe, H. Furuyama, S. Naritsuka, N. Sugiyama, Y. Kokubun, and M. Nakamura, "Effects of well number, cavity length, and facet reflectivity on the reduction of threshold current of GaAs/AlGaAs multiquantum well lasers," *IEEE Journal of Quantum Electronics*, vol. 24, no. 4, pp. 635–640, 1988.
- [14] G. P. Watson, D. G. Ast, T. J. Anderson, B. Pathangey, and Y. Hayakawa, "The measurement of deep level states caused by misfit dislocations in InGaAs/GaAs grown on patterned GaAs substrates," *Journal of Applied Physics*, vol. 71, no. 7, pp. 3399–3407, Apr. 1992.
- [15] G. C. Osbourn, P. L. Gourley, I. J. Fritz, R. M. Biefeld, L. R. Dawson, and T. E. Zipperian, "Chapter 8 principles and applications of semiconductor strained-layer superlattices," in *Semiconductors and Semimetals*, vol. Volume 24, Raymond Dingle, Ed. Elsevier, 1987, pp. 459–503.
- [16] P. J. A. Thijs, L. F. Tiemeijer, P. I. Kuindersma, J. J. M. Binsma, and T. Van Dongen, "High-performance 1.5 μm wavelength InGaAs-InGaAsP strained quantum well lasers and amplifiers," *IEEE Journal of Quantum Electronics*, vol. 27, no. 6, pp. 1426–1439, Jun. 1991.
- [17] J. W. Matthews and A. E. Blakeslee, "Defects in epitaxial multilayers," *Journal of Crystal Growth*, vol. 27, pp. 118–125, Dec. 1974.

- [18] K. J. Beernink, P. K. York, J. J. Coleman, R. G. Waters, J. Kim, and C. M. Wayman, "Characterization of InGaAs-GaAs strained-layer lasers with quantum wells near the critical thickness," *Applied Physics Letters*, vol. 55, no. 21, pp. 2167–2169, Nov. 1989.
- [19] T. M. Cockerill, D. V. Forbes, J. A. Dantzig, and J. J. Coleman, "Strained-layer InGaAs-GaAs-AlGaAs buried-heterostructure quantum-well lasers by three-step selective-area metalorganic chemical vapor deposition," *IEEE Journal of Quantum Electronics*, vol. 30, no. 2, pp. 441–445, Feb. 1994.
- [20] R. Dingle and C. H. Henry, "United States Patent: 3982207 - Quantum effects in heterostructure lasers," 398220721-Sep-1976.
- [21] Y. Arakawa and A. Yariv, "Theory of gain, modulation response, and spectral linewidth in AlGaAs quantum well lasers," *IEEE Journal of Quantum Electronics*, vol. 21, no. 10, pp. 1666–1674, Oct. 1985.
- [22] D. A. B. Miller, D. S. Chemla, T. C. Damen, A. C. Gossard, W. Wiegmann, T. H. Wood, and C. A. Burrus, "Electric field dependence of optical absorption near the band gap of quantum-well structures," *Physical Review B*, vol. 32, no. 2, pp. 1043–1060, Jul. 1985.
- [23] T. Ido, H. Sano, D. J. Moss, S. Tanaka, and A. Takai, "Strained InGaAs/InAlAs MQW electroabsorption modulators with large bandwidth and low driving voltage," *IEEE Photonics Technology Letters*, vol. 6, no. 10, pp. 1207–1209, Oct. 1994.
- [24] D. Moss, D. Landheer, A. Delage, F. Chatenoud, and M. Dion, "Laser compatible waveguide electroabsorption modulator with high contrast and low operating voltage in GaAs/AlGaAs," *IEEE Photonics Technology Letters*, vol. 3, no. 7, pp. 645–647, Jul. 1991.
- [25] T. L. Koch, U. Koren, G. Eisenstein, M. G. Young, M. Oron, C. R. Giles, and B. I. Miller, "Tapered waveguide InGaAs/InGaAsP multiple-quantum-well lasers," *IEEE Photonics Technology Letters*, vol. 2, no. 2, pp. 88–90, Feb. 1990.
- [26] R. M. Lammert, D. V. Forbes, G. M. Smith, M. L. Osowski, and J. J. Coleman, "InGaAs-GaAs quantum-well lasers with monolithically integrated intracavity electroabsorption modulators by selective-area MOCVD," *Photonics Technology Letters, IEEE*, vol. 8, no. 1, pp. 78–80, Jan. 1996.
- [27] A. E. Willner, Z. Pan, and M. I. Hayee, "Major accomplishments in 2010 on optical fiber communications," *IEEE Photonics Journal*, vol. 3, no. 2, pp. 320–324, 2011.
- [28] K. Utaka, K. Kobayashi, and Y. Suematsu, "Lasing characteristics of 1.5 - 1.6 μm GaInAsP/InP integrated twin-guide lasers with first-order distributed Bragg reflectors," *IEEE Journal of Quantum Electronics*, vol. 17, no. 5, pp. 651–658, May 1981.
- [29] J. Wallin, G. Landgren, K. Streubel, S. Nilsson, and M. Oberg, "Selective area regrowth of butt-joint coupled waveguides in multi-section DBR lasers," in *Metalorganic Vapor Phase Epitaxy, 1992. Sixth International Conference, 1992*, pp. 73–74.
- [30] T. L. Koch and U. Koren, "Semiconductor photonic integrated circuits," *IEEE Journal of Quantum Electronics*, vol. 27, no. 3, pp. 641–653, Mar. 1991.
- [31] T. Kitatani, K. Shinoda, T. Tsuchiya, H. Sato, K. Ouchi, H. Uchiyama, S. Tsuji, and M. Aoki, "Evaluation of the optical-coupling efficiency of InGaAlAs-InGaAsP butt joint using a novel multiple butt-jointed laser," *IEEE Photonics Technology Letters*, vol. 17, no. 6, pp. 1148–1150, Jun. 2005.
- [32] T. M. Cockerill, D. V. Forbes, H. Han, and J. J. Coleman, "Monolithic integration of a strained-layer InGaAs-GaAs-AlGaAs quantum-well laser with a passive waveguide by selective-area MOCVD," *Photonics Technology Letters, IEEE*, vol. 5, no. 4, pp. 448–450, Apr. 1993.
- [33] R. J. Deri, C. Caneau, E. Colas, L. M. Schiavone, N. C. Andreadakis, G. H. Song, and E. C. M. Pennings, "Integrated optic mode-size tapers by selective organometallic chemical vapor deposition of InGaAsP/InP," *Applied Physics Letters*, vol. 61, no. 8, pp. 952–954, 1992.
- [34] G. J. Davies, W. J. Duncan, P. J. Skevington, C. L. French, and J. S. Foord, "Selective area growth for opto-electronic integrated circuits (OEICs)," *Materials Science and Engineering: B*, vol. 9, no. 1–3, pp. 93–100, Jul. 1991.

- [35] T. Tanbun-Ek, Y. K. Chen, J. A. Grenko, E. K. Byrne, J. E. Johnson, R. A. Logan, A. Tate, A. M. Sergent, K. W. Wecht, P. F. Sciortine Jr., and S. N. G. Chu, "Integrated DFB-DBR laser modulator grown by selective area metalorganic vapor phase epitaxy growth technique," *Journal of Crystal Growth*, vol. 145, no. 1–4, pp. 902–906, Dec. 1994.
- [36] M. L. Osowski and J. J. Coleman, "Integrated photonic devices by selective-area MOCVD," in *SPIE 3290, Optoelectronic Integrated Circuits II*, 1997, pp. 8–19.
- [37] A. W. Nelson, W. J. Devlin, R. E. Hobbs, C. G. D. Lenton, and S. Wong, "High-power, low-threshold BH lasers operating at 1.52 μm grown entirely by MOVPE," *Electronics Letters*, vol. 21, no. 20, pp. 888–889, 1985.
- [38] R. Azoulay, N. Bouadma, J. C. Bouley, and L. Dugrand, "Selective MOCVD epitaxy for optoelectronic devices," *Journal of Crystal Growth*, vol. 55, no. 1, pp. 229–234, Oct. 1981.
- [39] A. M. Jones and J. J. Coleman, "Integrated optoelectronic devices by selective-area epitaxy," in *SPIE 2918, Emerging Components and Technologies for All-Optical Photonic Systems II*, 1997, pp. 146–154.
- [40] E. C. Nelson, N. L. Dias, K. P. Bassett, S. N. Dunham, V. Verma, M. Miyake, P. Wiltzius, J. A. Rogers, J. J. Coleman, X. Li, and P. V. Braun, "Epitaxial growth of three-dimensionally architected optoelectronic devices," *Nature Materials*, vol. 10, no. 9, pp. 676–681, 2011.
- [41] O. Kayser, "Selective growth of InP/GaInAs in LP-MOVPE and MOMB/CBE," *Journal of Crystal Growth*, vol. 107, no. 1–4, pp. 989–998, Jan. 1991.
- [42] M. Gibbon, J. P. Stagg, C. G. Cureton, E. J. Thrush, C. J. Jones, R. E. Mallard, R. E. Pritchard, N. Collis, and A. Chew, "Selective-area low-pressure MOCVD of GaInAsP and related materials on planar InP substrates," *Semiconductor Science and Technology*, vol. 8, no. 6, pp. 998–1010, Jun. 1993.
- [43] R. D. Dupuis, "AlGaAs-GaAs lasers grown by metalorganic chemical vapor deposition — A review," *Journal of Crystal Growth*, vol. 55, no. 1, pp. 213–222, Oct. 1981.
- [44] H. M. Manasevit, "Single-crystal GaAs on insulating substrate," *Applied Physics Letters*, vol. 12, no. 4, pp. 156–159, Feb. 1968.
- [45] L. M. Miller and J. J. Coleman, "Metalorganic chemical vapor deposition," *Critical Reviews in Solid State and Materials Sciences*, vol. 15, no. 1, pp. 1–26, 1988.
- [46] M. F. Zybur, S. H. Jones, J. M. Duva, and J. Durgavich, "A simplified model describing enhanced growth rates during vapor phase selective epitaxy," *JEM*, vol. 23, no. 10, pp. 1055–1059, Oct. 1994.
- [47] K. Yamaguchi and K. Okamoto, "Lateral supply mechanisms in selective metalorganic chemical vapor deposition," *Japanese Journal of Applied Physics*, vol. 32, no. Part 1, No. 4, pp. 1523–1527, 1993.
- [48] T. Shioda, M. Sugiyama, Y. Shimogaki, and Y. Nakano, "Prediction method for the bandgap profiles of InGaAsP multiple quantum well structures fabricated by selective area metal-organic vapor phase epitaxy," in *International Conference on Indium Phosphide and Related Materials*, 2005, pp. 464–467.
- [49] D. H. Reep, "Deposition of GaAs Epitaxial Layers by Organometallic CVD," *Journal of The Electrochemical Society*, vol. 130, no. 3, p. 675, 1983.
- [50] M. E. Coltrin and C. C. Mitchell, "Mass transport and kinetic limitations in MOCVD selective-area growth," *Journal of Crystal Growth*, vol. 254, no. 1–2, pp. 35–45, Jun. 2003.
- [51] H. Heinecke, E. Veuhoff, N. Pütz, M. Heyen, and P. Balk, "Kinetics of GaAs growth by low pressure MO-CVD," *Journal of Electronic Materials*, vol. 13, no. 5, pp. 815–830, Sep. 1984.
- [52] E. Colas, A. Shahar, B. D. Soole, W. J. Tomlinson, J. R. Hayes, C. Caneau, and R. Bhat, "Lateral and longitudinal patterning of semiconductor structures by crystal growth on nonplanar and dielectric-masked GaAs substrates: Application to thickness-modulated waveguide structures," *Journal of Crystal Growth*, vol. 107, no. 1–4, pp. 226–230, Jan. 1991.

- [53] M. Aoki, M. Suzuki, M. Takahashi, H. Sano, T. Ido, T. Kawano, and A. Takai, "High-speed (10 Gbit/s) and low-drive-voltage (1 V peak to peak) InGaAs/InGaAsP MQW electroabsorption-modulator integrated DFB laser with semi-insulating buried heterostructure," *Electronics Letters*, vol. 28, no. 12, p. 1157, 1992.
- [54] R. Bhat, "Current status of selective area epitaxy by OMCVD," *Journal of Crystal Growth*, vol. 120, no. 1–4, pp. 362–368, May 1992.
- [55] *FIDAP Fluid Dynamics Analysis Package*. Evanston, IL: Fluid Dynamics International, Inc, 1993.
- [56] A. M. Jones, M. L. Osowski, R. M. Lammert, J. A. Dantzig, and J. J. Coleman, "Growth, characterization, and modeling of ternary InGaAs-GaAs quantum wells by selective-area metalorganic chemical vapor deposition," *Journal of Electronic Materials*, vol. 24, no. 11, pp. 1631–1636, Nov. 1995.
- [57] M. Maassen, O. Kayser, R. Westphalen, F. E. G. Guimaraes, J. Geurts, J. Finders, and P. Balk, "Localized deposition of GaAs/GaN heterostructures using LP-MOVPE," *Journal of Electronic Materials*, vol. 21, no. 3, pp. 257–264, Mar. 1992.
- [58] C. Caneau, R. Bhat, C. C. Chang, K. Kash, and M. A. Koza, "Selective organometallic vapor phase epitaxy of Ga and In compounds: a comparison of TMIIn and TEGa versus TMIIn and TMGa," *Journal of Crystal Growth*, vol. 132, no. 3–4, pp. 364–370, Sep. 1993.
- [59] C. Caneau, R. Bhat, M. R. Frei, C. C. Chang, R. J. Deri, and M. A. Koza, "Studies on the selective OMVPE of (Ga,In)/(As,P)," *Journal of Crystal Growth*, vol. 124, no. 1–4, pp. 243–248, Nov. 1992.
- [60] J. E. Greenspan, C. Blaauw, B. Emmerstorfer, R. W. Glew, and I. Shih, "Analysis of a time-dependent supply mechanism in selective area growth by MOCVD," *Journal of Crystal Growth*, vol. 248, pp. 405–410, Feb. 2003.
- [61] N. Vodjdani, A. Lemarchand, and H. Paradan, "Parametric studies of GaAs growth by metalorganic molecular beam epitaxy," *Le Journal de Physique Colloques*, vol. 43, no. C5, pp. C5–339–C5–349, Dec. 1982.
- [62] A. Okamoto and K. Ohata, "Substrate temperature lowering in GaAs selective epitaxial growth by molecular-beam epitaxy," *Journal of Applied Physics*, vol. 66, no. 7, pp. 3413–3415, Oct. 1989.
- [63] A. Okamoto and K. Ohata, "Selective epitaxial growth of gallium arsenide by molecular beam epitaxy," *Applied Physics Letters*, vol. 51, no. 19, pp. 1512–1514, Nov. 1987.
- [64] G. J. Davies and D. A. Andrews, "Metalorganic molecular beam epitaxy (MOMBE)," *Chemtronics*, vol. 3, no. 1, pp. 3–16, 1988.
- [65] E. Tokumitsu, Y. Kudou, M. Konagai, and K. Takahashi, "Molecular beam epitaxial growth of GaAs using trimethylgallium as a Ga source," *Journal of Applied Physics*, vol. 55, no. 8, pp. 3163–3165, Apr. 1984.
- [66] J. Finders, J. Geurts, A. Kohl, M. Weyers, B. Opitz, O. Kayser, and P. Balk, "Composition of selectively grown In_xGa_{1-x}As structures from locally resolved Raman spectroscopy," *Journal of Crystal Growth*, vol. 107, no. 1–4, pp. 151–155, Jan. 1991.
- [67] W. T. Tsang, "Extremely low threshold (AlGa)As modified multiquantum well heterostructure lasers grown by molecular-beam epitaxy," *Applied Physics Letters*, vol. 39, no. 10, pp. 786–788, Nov. 1981.
- [68] T. Fujii, S. Hiyamizu, S. Yamakoshi, and T. Ishikawa, "MBE growth of extremely high quality GaAs - AlGaAs GRIN SCH lasers with a superlattice buffer layer," *Journal of Vacuum Science Technology B: Microelectronics and Nanometer Structures*, vol. 3, no. 2, pp. 776–778, 1985.
- [69] Y. Arakawa, K. Vahala, and A. Yariv, "Quantum noise and dynamics in quantum well and quantum wire lasers," *Applied Physics Letters*, vol. 45, no. 9, pp. 950–952, 1984.
- [70] R. Chin, N. Holonyak, B. A. Vojak, K. Hess, R. D. Dupuis, and P. D. Dapkus, "Temperature dependence of threshold current for quantum well Al_xGa_(1-x)As-GaAs heterostructure laser diodes," *Applied Physics Letters*, vol. 36, no. 1, pp. 19–21, 1980.

- [71] A. Yariv, *Optical Electronics*. New York: Oxford University Press, 1991.
- [72] J. Guthrie, G. L. Tan, M. Ohkubo, T. Fukushima, Y. Ikegami, T. Ijichi, M. Irikawa, R. S. Mand, and J. M. Xu, "Beam instability in 980-nm power lasers: Experiment and analysis," *IEEE Photonics Technology Letters*, vol. 6, no. 12, pp. 1409–1411, 1994.
- [73] A. E. Huber, T. S. Yeoh, R. B. Swint, C. Y. Woo, K. E. Lee, S. D. Roh, J. J. Coleman, B. O. Faircloth, and M. S. Zediker, "Novel design for high-power single-lateral-mode lasers," *IEEE Photonics Technology Letters*, vol. 13, no. 10, pp. 1064–1066, Oct. 2001.
- [74] T. L. Koch and J. E. Bowers, "Nature of wavelength chirping in directly modulated semiconductor lasers," *Electronics Letters*, vol. 20, no. 25, pp. 1038–1040, 1984.
- [75] M. K. Chin, "Comparative analysis of the performance limits of Franz-Keldysh effect and quantum-confined Stark effect electroabsorption waveguide modulators," *Optoelectronics, IEE Proceedings*, vol. 142, no. 2, pp. 109–114, 1995.
- [76] F. K. Reinhart and B. I. Miller, "Efficient GaAs/Al(x)Ga(1-x)As double-heterostructure light modulators," *Applied Physics Letters*, vol. 20, no. 1, pp. 36–38, Jan. 1972.
- [77] D. A. B. Miller, D. S. Chemla, T. C. Damen, A. C. Gossard, W. Wiegmann, T. H. Wood, and C. A. Burrus, "Band-edge electroabsorption in quantum well structures: The quantum-confined Stark effect," *Physical Review Letters*, vol. 53, no. 22, pp. 2173–2176, Nov. 1984.
- [78] S. W. Kirchoefer, N. Holonyak, K. Hess, D. A. Gulino, H. G. Drickamer, J. J. Coleman, and P. D. Dapkus, "Absorption measurements at high pressure on AlAs-Al(x)Ga(1-x)As-GaAs superlattices," *Applied Physics Letters*, vol. 40, no. 9, pp. 821–824, May 1982.
- [79] D. S. Chemla, D. A. B. Miller, P. W. Smith, A. C. Gossard, and W. Wiegmann, "Room temperature excitonic nonlinear absorption and refraction in GaAs/AlGaAs multiple quantum well structures," *IEEE Journal of Quantum Electronics*, vol. 20, no. 3, pp. 265–275, 1984.
- [80] P. J. Mares and S. L. Chuang, "Modeling of self-electro-optic-effect devices," *Journal of Applied Physics*, vol. 74, no. 2, pp. 1388–1397, Jul. 1993.
- [81] M. Goto, K. Hironishi, A. Sugata, K. Mori, T. Horimatsu, and M. Sasaki, "A 10-Gb/s optical transmitter module with a monolithically integrated electroabsorption modulator with a DFB laser," *IEEE Photonics Technology Letters*, vol. 2, no. 12, pp. 896–898, 1990.
- [82] R. M. Lammert, G. M. Smith, S. Hughes, M. L. Osowski, A. M. Jones, and J. J. Coleman, "MQW wavelength-tunable DBR lasers with monolithically integrated external cavity electroabsorption modulators with low-driving voltages fabricated by selective-area MOCVD," *IEEE Photonics Technology Letters*, vol. 8, no. 6, pp. 797–799, Jun. 1996.
- [83] M. Aoki, H. Sano, M. Suzuki, M. Takahashi, K. Uomi, and A. Takai, "Novel structure MQW electroabsorption modulator/DFB-laser integrated device fabricated by selective area MOCVD growth," *Electronics Letters*, vol. 27, no. 23, pp. 2138–2140, Nov. 1991.
- [84] Y. Miyazaki, T. Yamatoya, K. Matsumoto, K. Kuramoto, K. Shibata, T. Aoyagi, and T. Ishikawa, "High-power ultralow-chirp 10-Gb/s electroabsorption modulator integrated laser with ultrashort photocarrier lifetime," *IEEE Journal of Quantum Electronics*, vol. 42, no. 4, pp. 357–362, 2006.
- [85] E. Foti, L. Fratta, F. Ghiglieno, C. Coriasso, C. Cacciatore, C. Rigo, M. Agresti, M. Vallone, S. Codato, G. Fornuto, R. Fang, M. Rosso, A. Bucciari, and P. Valenti, "Optimisation of 10 Gbit/s InGaAsP electroabsorption modulator operating at high temperature," *Optoelectronics, IEE Proceedings*, vol. 151, no. 2, pp. 103–108, 2004.
- [86] W.-J. Choi, A. E. Bond, J. Kim, J. Zhang, R. Jambunathan, H. Foulk, S. O'Brien, J. Van Norman, D. Vandegrift, C. Wanamaker, J. Shakespeare, and H. Cao, "Low insertion loss and low dispersion penalty InGaAsP quantum-well high-speed electroabsorption modulator for 40-Gb/s very-short-reach, long-reach, and long-haul applications," *Journal of Lightwave Technology*, vol. 20, no. 12, pp. 2052–2056, 2002.

- [87] M. Birk, C. Skolnick, B. Curto, R. Marlieb, T. J. Schmidt, and R. Saunders, "Field trial of a 40 Gbit/s PSBT channel upgrade to an installed 1700 km 10 Gbit/s system," in *Optical Fiber Communication Conference, 2005. Technical Digest. OFC/NFOEC, 2005*, vol. 2, p. 3 pp.
- [88] D. Delprat, A. Ramdane, L. Silvestre, A. Ougazzaden, F. Delorme, and S. Slempek, "20-Gb/s integrated DBR laser-EA modulator by selective area growth for 1.55 μm WDM applications," *IEEE Photonics Technology Letters*, vol. 9, no. 7, pp. 898–900, Jul. 1997.
- [89] N. Dupuis, J. Decobert, P.-Y. Lagree, N. Lagay, F. Poingt, C. Kazmierski, A. Ramdane, and A. Ougazzaden, "Mask pattern interference in AlGaInAs selective area metal-organic vapor-phase epitaxy: Experimental and modeling analysis," *Journal of Applied Physics*, vol. 103, no. 11, pp. 113113–113113–8, 2008.
- [90] L. K. Lee, T. Jung, and P.-C. Ku, "Photoluminescence study of InGaN site-controlled nanostructures formed by selective area epitaxy," in *IEEE Lasers and Electro-Optics Society, 2008. LEOS 2008. 21st Annual Meeting of the*, 2008, pp. 433–434.
- [91] D. Y. Song, A. Chandolu, N. Stojanovic, S. A. Nikishin, and M. Holtz, "Effect of impurity incorporation on emission wavelength in cathodoluminescence spectrum image study of GaN pyramids grown by selective area epitaxy," *Journal of Applied Physics*, vol. 104, no. 6, pp. 064309–064309–4, Sep. 2008.
- [92] N. Gogneau, L. Le Gratiet, E. Cambril, G. Beaudoin, G. Patriarche, A. Beveratos, R. Hostein, I. Robert-Philip, and I. Sagnes, "One step nano selective area growth of localized InAs/InP quantum dots for single photon source applications," in *20th International Conference on Indium Phosphide and Related Materials*, 2008, pp. 1–4.
- [93] K. Tomioka, Y. Kobayashi, J. Motohisa, S. Hara, and T. Fukui, "Selective-area growth of vertically aligned GaAs and GaAs/AlGaAs core-shell nanowires on Si(111) substrate," *Nanotechnology*, vol. 20, no. 14, p. 145302, Apr. 2009.
- [94] L. J. Mawst, J. H. Park, J. Kirch, C.-C. Liu, M. K. Rathi, P. F. Nealey, and T. F. Kuech, "Controlled growth of InGaAs/InGaAsP/InP Quantum Dots using diblock copolymer lithography and selective area MOCVD growth," in *IEEE LEOS Annual Meeting Conference Proceedings, 2009. LEOS '09*, 2009, pp. 739–740.
- [95] O. Madelung, *Semiconductors*. Berlin; New York: Springer-Verlag, 1991.